Article

Estimation of Land Surface Temperature in an Agricultural Region of Bangladesh from Landsat 8: Intercomparison of Four Algorithms

Md Qutub Uddin Sajib [1,†] and **Tao Wang** [1,*,†]

School of Environmental Studies, China University of Geosciences, Wuhan 430078, China; qsajib71@gmail.com
* Correspondence: twang21@cug.edu.cn
† These authors contributed equally to this work.

check for updates

Abstract: The presence of two thermal bands in Landsat 8 brings the opportunity to use either one or both of these bands to retrieve Land Surface Temperature (LST). In order to compare the performances of existing algorithms, we used four methods to retrieve LST from Landsat 8 and made an intercomparison among them. Apart from the direct use of the Radiative Transfer Equation (RTE), Single-Channel Algorithm and two Split-Window Algorithms were used taking an agricultural region in Bangladesh as the study area. The LSTs retrieved in the four methods were validated in two ways: first, an indirect validation against reference LST, which was obtained in the Atmospheric and Topographic CORrection (ATCOR) software module; second, cross-validation with Terra MODerate Resolution Imaging Spectroradiometer (MODIS) daily LSTs that were obtained from the **App**lication for **E**xtracting and **E**xploring **A**nalysis **R**eady **S**amples (A$\rho\rho$EEARS) online tool. Due to the absence of LST-monitoring radiosounding instruments surrounding the study area, in situ LSTs were not available; hence, validation of satellite retrieved LSTs against in situ LSTs was not performed. The atmospheric parameters necessary for the RTE-based method, as well as for other methods, were calculated from the National Centers for Environmental Prediction (NCEP) database using an online atmospheric correction calculator with MODerate resolution atmospheric TRANsmission (MODTRAN) codes. Root-mean-squared-error (RMSE) against reference LST, as well as mean bias error against both reference and MODIS daily LSTs, was used to interpret the relative accuracy of LST results. All four methods were found to result in acceptable LST products, leaving atmospheric water vapor content (w) as the important determinant for the precision result. Considering a set of several Landsat 8 images of different dates, Jiménez-Muñoz et al.'s (2014) Split-Window algorithm was found to result in the lowest mean RMSE of 1.19 °C. Du et al.'s (2015) Split-Window algorithm resulted in mean RMSE of 1.50 °C. The RTE-based direct method and the Single-Channel algorithm provided the mean RMSE of 2.47 °C and 4.11 °C, respectively. For Du et al.'s algorithm, the w range of 0.0 to 6.3 g cm^{-2} was considered, whereas for the other three methods, w values as retrieved from the NCEP database were considered for corresponding images. Land surface emissivity was retrieved through the Normalized Difference Vegetation Index (NDVI)-threshold method. This intercomparison study provides an LST retrieval methodology for Landsat 8 that involves four algorithms. It proves that (i) better LST results can be obtained using both thermal bands of Landsat 8; (ii) the NCEP database can be used to determine atmospheric parameters using the online calculator; (iii) MODIS daily LSTs from A$\rho\rho$EEARS can be used efficiently in cross-validation and intercomparison of Landsat 8 LST algorithms; and (iv) when in situ LST data are not available, the ATCOR-derived LSTs can be used for indirect verification and intercomparison of Landsat 8 LST algorithms.

1. Introduction

Estimation of Land Surface Temperature (LST) and the study of its changes over time is an important topic of research because, these days, global climate is changing fast. Therefore, retrieval of LST with new technologies has become an interesting field to explore in order to better understand the environment all over the world. With the recent advancement in remote sensing earth observation systems, studying LST, as well as land use and land cover (LULC), has become much easier than it was before. Today, many sources of satellite images are available containing optical, as well as thermal, information of earth surfaces.

LST is the thermodynamic skin temperature of land surfaces which can be studied by measuring the infrared radiation coming from the surface [1]. With LST information, urban heat island can be monitored [2,3] and forest fire can be detected [4]. LST information can be useful to estimate the soil moisture [5–7]; hence, studies related to many hydrological processes can be explored from LST [8]. It can also help in different climate studies and weather forecast [8–10]. Changes in LST over time can be related with changes in LULC types [11]. LST is related with all sorts of processes that control the energy and water fluxes over the interfaces between the Earth's surface and the atmosphere [12,13]. All these applications make the study of LST a crucial parameter to better understand the regional, as well as the global, environment and its changes over time.

There are different algorithms proposed for the retrieval of LST using different sources of Remote Sensing (RS) data [14–20]. Among those sources, Landsat has the biggest archive of free images and are of great interest among researches for LST study. Studies with Landsat data include LST retrieval with Landsat 5 TM (Thematic Mapper) data over an agricultural region of Spain by Sobrino et al. [21]; LST with Landsat 7 ETM+ (Enhanced Thematic Mapper Plus) data over Maraqeh County of Iran [22]; and, a work by Fu and Weng [23] for consistent and daily LST monitoring using Landsat images from 1984 to 2011 over the Beijing city of China. Mallick et al. [24] used Landsat 7 ETM+ data to perform LULC and LST study over a heterogeneous urban area of India. Sahana et al. [25] studied LULC change and its impact on LST using Landsat 5 TM data and Landsat 8 thermal infrared (TIR) data over the Sundarban biosphere reserve in India.

Study of LST with RS data over different areas in Bangladesh is rather limited compared to other countries of the world. Bangladesh covers an area of 147,570 km^2 [26] with a huge population. Geographically it extends from 20°34′ N to 26°38′ N latitude and from 88°1′ E to 92°41′ E longitude [26]. It is one of the most densely populated countries in the world [27]. Most of its population live in its capital city. An agricultural region close to the capital city was selected as the study area for this work (see Section 2.2).

Speaking of the limited LST research works in Bangladesh, those found in literature include the capital city and some of its surrounding areas [28–30], and at least one work covering the whole country [31]. Changes in LST and land cover over time, as well as future LST simulation, was studied by Ahmed et al. [28] in the capital city of Bangladesh using Landsat 4, 5 TM, and Landsat 7 ETM+ data. Reja [29] retrieved LST using Landsat 4 TM and Landsat 7 ETM+ data. Sultana et al. [31] used NOAA-16 (National Oceanic and Atmospheric Administration - 16) and NOAA-17 data to estimate the minimum and maximum LSTs for six different seasons of whole country. Roni [30] studied the relation between LST and Normalized Difference Vegetation Index (NDVI) using Landsat TM data. Ara et al. [32] used Landsat 8, along with Landsat TM and ETM+ data, to study the effects of land use intensity on LST in Chittagong city corporation area. Study of LST with Landsat 8 images in the capital city or its surrounding areas in Bangladesh is not known as of the time of writing this paper.

Retrieval of LST with the precision result depends on data type, environmental conditions, and the particular algorithm used for the calculation. LST retrieval algorithms may depend on the presence of one or multiple thermal bands in the source RS data. Thermal channel in electromagnetic spectrum covers the region of 10 to 12 µm. Previous Landsat missions came with only one thermal channel but Landsat 8 has two. Sensors with more than one thermal band allow the user to extract information from both of these bands with the possibility of better LST retrieval.

Geostationary satellites/platforms, such as SEVIRI (Spinning Enhanced Visible and Infrared Imager), can be used to retrieve surface emissivity and temperature simultaneously by using Kalman filter strategy [33]. The retrieval process is physical-based and can be applied for both land- and sea-surface temperatures with very good results compared with LST from non-geostationary satellite observations [34]. The same Kalman filter methodology can be found to produce a very good result in different land cover types, including arid, cultivated, and vegetated, as well as urban, areas and sea water [35].

In this study, we used four algorithms—a Single-Channel Algorithm [36,37], two Split-Window algorithms [37–40], and a direct method based on the Radiative Transfer Equation (RTE) [41,42]—to retrieve LST from Landsat 8 data. All these algorithms were used for LST retrieval on a study area covered mostly with vegetative land surfaces. Located in Bangladesh with subtropical climatic conditions, the selected area during the period of study (February 2018) experiences pleasantly sunny winter with minimal to no precipitation and mostly clear to partly cloudy sky conditions. All four algorithms for Landsat 8 in this study area were found providing with acceptable LST results compared with reference LSTs and MODerate Resolution Imaging Spectroradiometer (MODIS) daily LSTs, while the Split-Window algorithms performed better than the other two (see Section 4). Based on the LST results from the four methods, an intercomparison among them was made. A cross-validation study of LSTs obtained from Landsat 8 images was performed against MODIS daily LST data. At 1 km spatial resolution, the MODIS images produce global daily LST data [43]; hence, it can be used for cross-validation of Landsat LST products. Available online at https://lpdaacsvc.cr.usgs.gov/appeears/, the **App**lication for **E**xtracting and **E**xploring **A**nalysis **R**eady **S**amples (A$\rho\rho$EEARS) can be used to extract daily or 8-day composite MODIS LSTs [44,45].

This paper is organized as follows: Section 2 describes materials and methods, including the details about remote sensing data used in this study. A unified methodology flowchart involving different steps in LST retrieval with four algorithms is also presented in this section. Section 3 provides the theoretical aspects of LST study from Landsat 8 with brief description of four algorithms. It also describes the estimation of normalized difference vegetation index, proportion of vegetation cover, land surface emissivity, top-of-atmosphere (ToA) brightness temperature, and the processing of input data for LST algorithms. Section 4 presents the results of LSTs retrieved with four algorithms, including their validation results against reference LST, as well as the intercomparison study, among them. Results from the cross-validation study of Landsat 8 LSTs against MODIS daily LSTs are also presented in this section. Section 5 summarizes the findings and concluding remarks of this work.

Mathematical notations of parameters involved in LST determination are found in literature with not-so-uniform expressions. In this paper, $T_{\text{ToA},i}$ denotes the top-of-atmosphere (ToA, or at-sensor) brightness temperature for channel i; $L_{\text{ToA},i}$ is the ToA spectral radiance for channel i; $B_i(T_i)$ is the ToA thermal radiance; $\rho_{\lambda,\text{LS}}$ is the reflectance from the surface; LSE_i is the Land Surface Emissivity for band i; and P_{v} is the proportion of vegetation. Because of the stray light effect observed in band 11 images of Landsat 8 [46,47], we used RTE-based direct method and Single-Channel method for band 10 only. In Split-Window algorithms, however, both thermal bands were used.

2. Materials and Methods

Landsat 8 images were used as the primary sources of data to retrieve the LST products. Two Split-Window algorithms, a Single-Channel Algorithm, and an RTE-based direct method were used. The Landsat 8 satellite-retrieved LST products obtained in four methods were validated against reference LSTs and MODIS daily LSTs. The idea is to perform an intercomparison, and study the relative performances of four existing LST algorithms from Landsat 8. The reference LST was retrieved with the Atmospheric and Topographic CORection (ATCOR) module. The MODIS daily LST products were extracted using the A$\rho\rho$EEARS online tool. A study area in an agricultural region of Bangladesh was selected for this research.

2.1. Dataset

Landsat 8, the primary source of data in this work, travels on the descending (daytime) node from north to south and crosses the equator at 10:11 a.m. ±15 min mean local time. For our study area, primarily one Landsat 8 image was downloaded from the USGS earth explorer website. The image was taken on 21 February 2018—the actual date on which the authors conducted a field work in the study area—with Operational Land Imager (OLI) and Thermal Infrared (TIR) scanners onboard Landsat 8, and has Path 137 and Row 44. The TIR bands were used to retrieve LSTs, along with the red (band 4) and infrared (band 5) channels for estimating NDVI. The shapefiles necessary for our study were downloaded from the Database of Global Administrative Areas (GADM—https://gadm.org/).

In order to test the LST algorithms on other Landsat 8 images, a set of four Landsat 8 scenes of different dates were downloaded. Two of them were images taken before 21 February 2018, while the other two images were taken after 21 February. We did not use the image of 5 February 2018 because this image was found covered with 77.4% cloud. The amount of cloud cover in percentage is available in the Landsat 8 image metadata file as `CLOUD_COVER`. The approach used for the cloud classification in Landsat 8 images involve multiple algorithms. It is collectively known as the Cloud Cover Assessment (CCA) and includes the Automated Cloud Cover (ACCA), See-5 CCA, Cirrus CCA, AT-ACCA, etc., algorithms [48] to classify clouds. The CCA analysis results are then merged into the final L1 quality band and the cloud cover amount is made available in the image metadata file. Further details regarding the cloud detection algorithms of Landsat 8 can be found in Reference [48].

To perform cross-validation of Landsat 8 LST products with MODIS daily LST data, we downloaded Terra MODIS LST products using the A$\rho\rho$EEARS online application. We extracted the daily MODIS LSTs of different dates by uploading the shapefiles of our study area in the online module. Details of all Landsat 8 and MODIS images used in this study are presented in Table 1.

Table 1. Landsat 8 and Terra MODerate Resolution Imaging Spectroradiometer (MODIS) image data used in this study.

| Landsat 8 Images				MODIS Images		
Image Date	Scene Identifier	Path	Row	Image Date	Identifier	Data Type
4 January 2018	LC81370442018004LGN00	137	44	5 January 2018	MOD11A1.006	LST_Day_1km
20 January 2018	LC81370442018020LGN00	137	44	21 January 2018	MOD11A1.006	LST_Day_1km
21 February 2018	LC81370442018052LGN00	137	44	22 February 2018	MOD11A1.006	LST_Day_1km
9 March 2018	LC81370442018068LGN00	137	44	10 March 2018	MOD11A1.006	LST_Day_1km
25 March 2018	LC81370442018084LGN00	137	44	26 March 2018	MOD11A1.006	LST_Day_1km

2.2. Study Area

The study area selected for the verification and intercomparison of four LST algorithms is Chandina sub-district under Cumilla district in Bangladesh. Cumilla district is adjacent to the capital city of Bangladesh. Located in South Asia, Bangladesh is virtually surrounded by India and the Bay of Bengal to the south [49]. It is a low-lying country with huge count of rivers.

Cumilla district is situated in the south eastern part of Bangladesh [50]. It has an area of 3085.17 km^2, and located in between 23°2′ N to 24°47′ N latitudes and in between 92°39′ E to 91°22′ E longitudes [51]. There are 17 *Upazilas* (sub-districts) in this district, among which Chandina is one. Figure 1 shows the location of this sub-district as our study area.

Chandina sub-district is an area of about 201 km^2, with mostly vegetative land surfaces. A visit to the study area was arranged as part of this research, and it was found that different types of vegetables are grown in this area.

The study area observation was conducted in two consecutive days, 21 and 22 February in 2018, under clear sky conditions, starting the visit in the morning at around 8:30 local time till 15:30 in the afternoon. There were no radiosounding instruments available surrounding the study area; hence, in situ LST data were not monitored. It was found that the local experts usually monitor the LST with

soil thermometers in these areas, which may not be a good measurement of in situ LSTs compared to radiometer-retrieved in situ LSTs. Therefore, the intercomparison study of four LST algorithms from Landsat 8 was carried out against ATCOR-derived reference LSTs and A$\rho\rho$EEARS-derived MODIS daily LSTs.
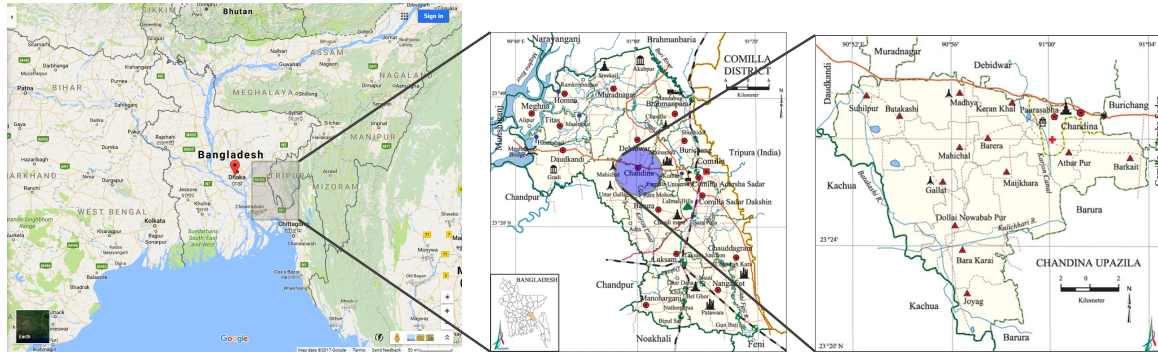
Figure 1. Chandina sub-district of Cumilla district in Bangladesh (from left to right, not to scale). Compiled from References [50–52].

2.3. Research Methodology

The methodology to perform the intercomparison of different LST algorithms requires the estimation of LSTs from Landsat 8 images using each of these algorithms. A flowchart representing different steps in LST estimation with four algorithms is shown in Figure 2. As shown in this flowchart, processing of the remote sensing data starts with the level-1 product of Landsat 8 images. Then, the first step is to remove the cloud and haze from level-1 DN values, which is a part of the atmospheric correction. In this study, we used the ATCOR module for atmospheric correction, which uses MODerate resolution atmospheric TRANsmission (MODTRAN) codes to classify and remove cloud and haze from a Landsat 8 scene.

Once the remote sensing images are atmospherically corrected, both optical (OLI) and thermal (TIR) bands are necessary to determine the LST. Using optical bands, band 4 (red) and band 5 (infrared) in particular, NDVI is estimated. From the NDVI, first the proportion of vegetation (P_v), then land surface emissivity (LSE) is determined.

Using both thermal bands of Landsat 8 data, top-of-atmosphere radiance (L_{ToA}) is first determined. Then, top-of-atmosphere temperature (T_{ToA}) is estimated. After that, using appropriate LST algorithm with its mathematical formula and its coefficient values (see Section 3), LST can be retrieved using emissivity and T_{ToA} as shown in the flowchart.

Once LSTs with different algorithms are estimated, they can be validated against in situ LSTs or reference LSTs. In this study, the algorithm-retrieved LSTs from Landsat 8 were validated comparing them with reference LSTs retrieved using the ATCOR module. Validation of algorithm-retrieved LST against ATCOR-retrieved LST can be called as indirect verification [53]. The indirect verification was chosen because the in situ LST data were not available due to the absence of radiosounding instruments in the study area. In addition to the indirect verification, cross-validation of Landsat 8 LSTs obtained from different algorithms was performed comparing them with MODIS daily LSTs. Intercomparison study of four Landsat 8 LST algorithms was performed against reference LSTs and MODIS daily LSTs.
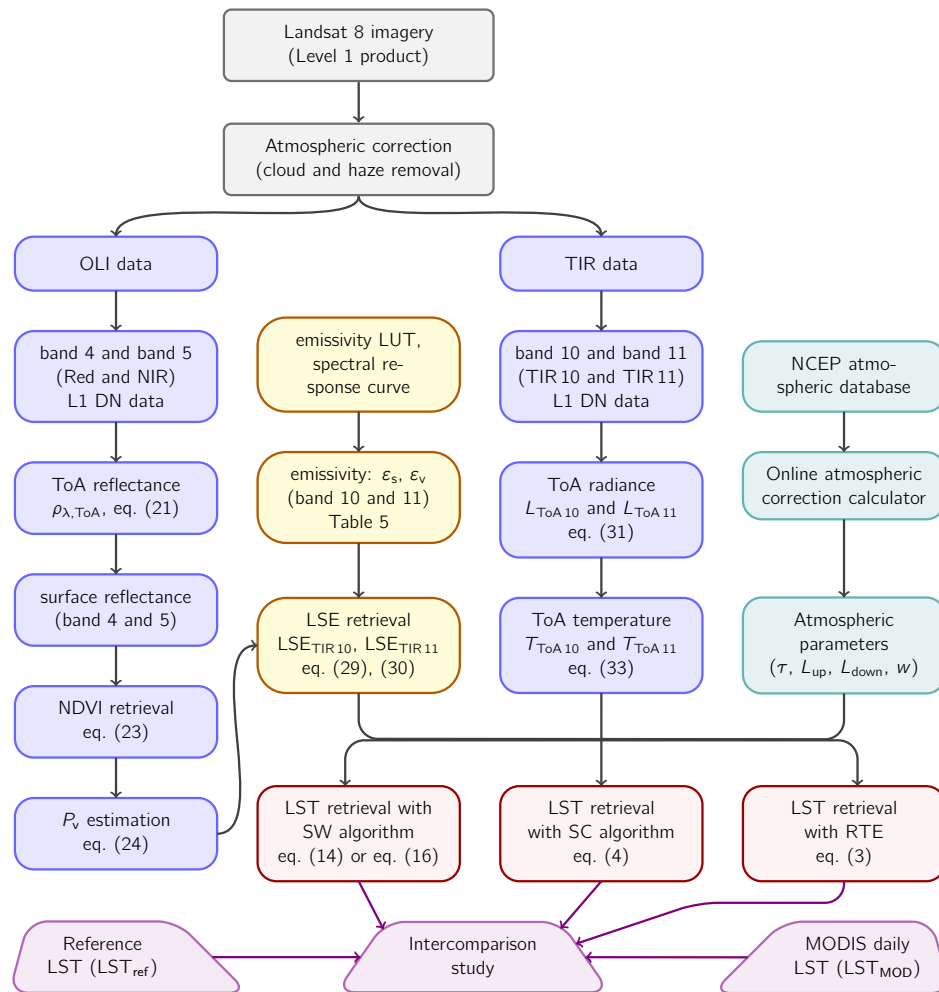
Figure 2. Algorithm flowchart for Land Surface Temperature (LST) retrieval with four methods and their intercomparison study from Landsat 8 thermal infrared (TIR) data. OLI = Operational Land Imager; LUT = Look Up Table ; DN = Digital Number; NDVI = Normalized Difference Vegetation Index; SW = Split-Window; NCEP = National Centers for Environmental Prediction; ToA = Top-of-Atmosphere; NIR = Near-Infrared; LSE = Land Surface Emissivity; SC = Single-Channel; TIR = Thermal Infrared.

3. Four Methods to Retrieve Land Surface Temperature from Landsat 8

The thermal channels of Landsat 8 images are band 10 and band 11, also known as TIR 1 and TIR 2 channels, respectively. First of these two has thermal window of 10.60 to 11.19 μm, and the latter 11.50 to 12.51 μm [48]. Since objects or land surfaces transmit radiation in different amounts depending on the wavelength of the channel window, reflected radiation recorded from two thermal bands contain different information about the land surface.

Retrieval methods of LST from thermal bands are based on the Radiative Transfer Equation (RTE). This equation can be used directly to estimate LST; or Single-Channel, Split-Window etc. methods can be used. The RTE-based direct method requires the information of atmospheric parameters for the study area. On the other hand, Single-Channel or Split-Window methods do not require the direct input of those parameters but use some coefficient values obtained through simulation calculations.

While LST can be estimated using one thermal band, the calculation of differential absorption in multiple TIR bands minimizes the atmospheric effects and has the potential to provide better results compared to the use of one thermal band [54]. This idea of using more than one thermal bands is called Split-Window technique [10,14]. Split-Window algorithms for Landsat 8 thermal bands were proposed by many researchers including Rozenstein et al. [55], Jiménez-Muñoz et al. [37], Yu et al. [41], and Du

et al. [40]. In this study, we used Split-Window algorithms developed by Jiménez-Muñoz et al. [37] and by Du et al. [40] because: (i) these two algorithms were found providing good performances in different w ranges [40], and (ii) first of these two requires direct input of w value, whereas the second comes with algorithm coefficients for several w sub-ranges. Therefore, it would be interesting to see how these two algorithms perform by making use of w in different ways.

When a Single-Channel or Split-Window algorithm is developed, using the MODerate resolution atmospheric TRANsmission (MODTRAN) or other radiative transfer codes, algorithm coefficients are estimated and made available to users so that they can be input directly in the mathematical expression of the algorithm to study LST for different areas of the world. Among various atmospheric profile databases that can be used in MODTRAN codes, examples include the Thermodynamic Initial Guess Retrieval (TIGR) profile constructed by the Laboratoire de Météorologie Dynamique [40], the Global Atmospheric Profiles from Reanalysis Information (GAPRI) database [37,56], the SAFREE database and the Cloudless Land Atmosphere Radiosounding (CLAR) database [56], the National Centers for Environmental Prediction (NCEP) database [57], etc.

The MODTRAN radiative transfer codes take atmospheric parameters and surface parameters as inputs. Spectral parameters needed for the MODTRAN codes are obtained from the spectral response functions of given TIR sensors [37,40,58]. Surface parameters for the MODTRAN codes may include emissivity [57], viewing geometry, etc. The atmospheric parameters retrieved from these codes include the transmittance (τ), up-welling path radiance (L_{up}), and down-welling path radiance (L_{down}) for the given thermal channel. In the following, we provide short description of four LST retrieval methods for Landsat 8 that were used for intercomparison in this study.

3.1. Radiative Transfer Equation and Atmospheric Parameters to Retrieve Land Surface Temperature

The formula to retrieve land surface temperature using Radiative Transfer Equation (RTE) can be expressed as [41]:

$$\text{LST} = \frac{c_2}{\lambda_i \cdot \ln\left(\frac{c_1 \cdot \tau_i \varepsilon_i}{\lambda_i^5 \cdot \left(B_i(T_i) - L_{\text{up}} - \tau_i(1-\varepsilon_i) \cdot L_{\text{down}}\right)} + 1\right)}, \tag{1}$$

where λ_i is the effective wavelength of band i; $B_i(T_i)$ is the ToA thermal radiance, τ_i is the band average atmospheric transmittance, and ε_i is the emissivity of the same band; L_{up} and L_{down} are the upwelling and downwelling radiance in the atmosphere obtained in band i; c_1 and c_2 are Planck's first and second radiation constants, respectively, with $c_1 = 1.191\,04 \times 10^8 \, \text{W} \, \mu\text{m}^4 \, \text{m}^{-2} \, \text{sr}^{-1}$ and $c_2 = 1.438\,77 \times 10^4 \, \mu\text{m} \, \text{K}$. To retrieve LST with RTE using Equation (1) three atmospheric parameters are needed: τ_i, L_{up}, and L_{down}; besides these parameters, land surface emissivity (ε_i) is necessary.

The λ_i in Equation (1) (or λ_{eff}) for a given band can be estimated as [41,42]:

$$\lambda_{\text{eff}} = \frac{\int_{\lambda_1}^{\lambda_2} \lambda \, f(\lambda) \, d\lambda}{\int_{\lambda_1}^{\lambda_2} f(\lambda) \, d\lambda}, \tag{2}$$

where $f(\lambda)$ is calculated as the function of the spectral responsivity of thermal bands; λ_1 and λ_2 are the lower and upper limit of $f(\lambda)$. As shown in Figure 3, the λ_{eff} for Landsat 8 band 10 is 10.8 μm and for band 11 is 12 μm.

For Landsat 8 TIR band 10, Equation (1) can be rewritten as

$$\text{LST} = \frac{c_2}{\lambda_{\text{eff,TIR10}} \cdot \ln\left(\frac{c_1 \cdot \tau_{\text{TIR10}} \cdot \text{LSE}_{\text{TIR10}}}{\lambda_{\text{eff}}^5 \cdot \left(L_{\text{ToA 10}} - L_{\text{up}} - \tau_{\text{TIR10}}(1 - \text{LSE}_{\text{TIR10}}) \cdot L_{\text{down}}\right)} + 1\right)}. \tag{3}$$

The atmospheric parameters needed to retrieve LST using Equation (3) can be estimated with local radiosounding instruments (if available) or from global atmospheric profiles using simulation codes.
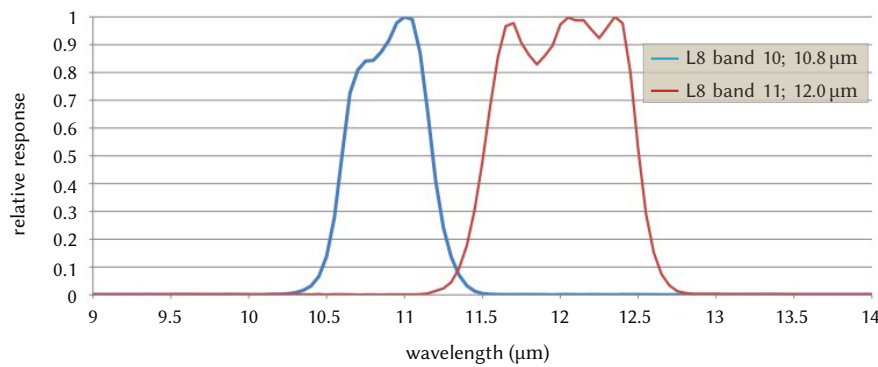
Figure 3. Effective wavelengths of Landsat 8 TIRS bands; 10.8 µm for TIR band 10, and 12 µm for TIR band 11. Source: Reference [59] (relabeled by the authors).

The online atmospheric correction calculator used in this study to estimate atmospheric parameters is available at https://atmcorr.gsfc.nasa.gov/ [57,60]. This calculator extracts required parameters from NCEP database using MODTRAN codes and spectral response curve of Landsat 8, Landsat 7, or Landsat 6. Coll et al. [61] have validated this web-based tool against ground measurements for Landsat 7 and reported that the atmospheric correction from this tool is comparable with correction from local radiosonde profiles. The tool was also used to validate a newly proposed pixel-by-pixel atmospheric correction method called SBAC for Landsat 7 in Reference [62]. The online atmospheric correction tool requires the user to input some mandatory data including location (longitude and latitude), date, and time for which the atmospheric parameters are to calculate. Optionally some surface conditions can be input, but if left empty, are assumed from the atmospheric database. The calculated parameters (τ_i, L_{up}, and L_{down}) are sent to the user via email.

3.2. Single-Channel Algorithm by Jiménez-Muñoz et al. (2014) with Coefficients

In the Single-Channel algorithm, only one thermal band is used to retrieve LST. For Landsat 8, either band 10 or band 11 can be used. The SC algorithm used in this study was developed by Jiménez-Muñoz and Sobrino [36] and was validated for AVHRR channels 4 and 5, ATSR2 channels 1 and 2, and Landsat TM band 6 data. Later this method was adapted for Landsat 8 by Jiménez-Muñoz et al. [37]. According to them, the SC algorithm for Landsat 8 can be expressed as

$$\text{LST} = \gamma \left[\frac{1}{\varepsilon} (\psi_1 L_{\lambda,\,\text{ToA}} + \psi_2) + \psi_3 \right] + \delta, \tag{4}$$

where ε is the land surface emissivity (LSE); ψ_1, ψ_2, and ψ_3 are atmospheric functions (AFs). The symbols δ and γ represent two parameters that can be estimated from linear approximation of Planck functions as [21]:

$$\gamma = \left\{ \frac{c_2 \cdot L_{\lambda,\text{ToA}}}{T_{\text{ToA}}^2} \left[\frac{\lambda^4 \cdot L_{\lambda,\text{ToA}}}{c_1} + \frac{1}{\lambda} \right] \right\}^{-1}. \tag{5}$$

The above equation can be rewritten for simplification as

$$\gamma = \frac{c_1 \cdot \lambda \cdot T_{\text{ToA}}^2}{c_2 \cdot L_{\lambda,\text{ToA}} (\lambda^5 \cdot L_{\lambda,\text{ToA}} + c_1)}, \tag{6}$$

where c_1, c_2, and λ holds same meaning as described in Section 3.1. The parameter δ in Equation (4) can be calculated according to Reference [21] as

$$\delta = -\gamma \cdot L_{\lambda,\text{ToA}} + T_{\text{ToA}}. \tag{7}$$

The AFs (ψ_1, ψ_2, and ψ_3) can be approximated with a second-order polynomial fit against atmospheric column water vapor content (w). If atmospheric function Ψ is considered as a function of water vapor content W as $\Psi = CW$, the matrix notation to determine the values of AFs can be expressed according to Reference [42] as

$$\begin{bmatrix} \psi_1 \\ \psi_2 \\ \psi_3 \end{bmatrix} = \begin{bmatrix} c_{11} & c_{12} & c_{13} \\ c_{21} & c_{22} & c_{23} \\ c_{31} & c_{32} & c_{33} \end{bmatrix} \begin{bmatrix} w^2 \\ w \\ 1 \end{bmatrix}, \tag{8}$$

where c_{ij} are coefficients that were determined by Jiménez-Muñoz et al. [37] for Landsat 8 TIR band 10 using the GAPRI_4838 database as

$$C = \begin{bmatrix} 0.04019 & 0.02916 & 1.01523 \\ -0.38333 & -1.50294 & 0.20324 \\ 0.00918 & 1.36072 & -0.27514 \end{bmatrix}. \tag{9}$$

Combining Equations (8) and (9), we can write

$$\psi_1 = 0.04019w^2 + 0.02916w + 1.01523, \tag{10}$$

$$\psi_2 = -0.38333w^2 - 1.50294w + 0.20324, \tag{11}$$

$$\psi_3 = 0.00918w^2 + 1.36072w - 0.27514. \tag{12}$$

Using Equations (10)–(12), for a given water vapor content (w) the atmospheric functions (AFs) for Single-Channel algorithm can be calculated and then input in the algorithm expressed in Equation (4) to retrieve LST from Landsat 8. Considering different amounts of water vapor content (w), the values for ψ_1, ψ_2, and ψ_3 can be calculated as shown in Table 2.

It should be mentioned here that the Equation (4) gives LST products in K (Kelvin) unit when Equation 32 is used to calculate the ToA brightness temperature (T_{ToA}). In order to get the LST in °C (degree Celsius) unit, the T_{ToA} needs to be calculated in °C unit using Equation 33, which involves the subtraction of 273.15. This T_{ToA} should then be used to compute the γ and δ parameters. Another way to get the LST products in °C unit is to subtract 273.15 directly in Equation (4).

Table 2. Atmospheric functions calculated for different amount of water vapor contents following Equations (10)–(12).

w (g cm^{-2})	ψ_1	ψ_2	ψ_3
0.5	1.039858	−0.6440625	0.407515
1.0	1.08458	−1.68303	1.09476
1.5	1.149398	−2.913663	1.786595
2.0	1.23431	−4.33596	2.48302
2.5	1.339317	−5.949922	3.184035
3.0	1.46442	−7.75555	3.88964
3.5	1.609618	−9.752843	4.599835
4.0	1.77491	−11.9418	5.31462
4.5	1.960298	−14.32242	6.033995

3.3. Split-Window Algorithm by Jiménez-Muñoz et al. (2014) with Coefficients

The Split-Window Algorithm by Jiménez-Muñoz et al. (2014) is based on the mathematical structure by Sobrino et al. [38]; it was later modified by Sobrino and Raissouni [63]. The same mathematical expression was used by Jiménez-Muñoz and Sobrino [58] to retrieve LST from different low-resolution thermal data. Then, it was adapted for Landsat 8 by Jiménez-Muñoz et al. [37]. According to this Split-Window algorithm, LST can be estimated with the following expression:

$$\text{LST} = T_i + c_0 + c_1\left(T_i - T_j\right) + c_2\left(T_i - T_j\right)^2 + \left(c_3 + c_4 w\right)\left(1 - \varepsilon_\text{m}\right) + \left(c_5 + c_6 w\right)\Delta\varepsilon, \tag{13}$$

where T_i and T_j are ToA brightness temperature for band i and band j. For Landsat 8, these two bands are band 10 and band 11, respectively; ε_m is the mean land surface emissivity of two bands and is calculated with $\frac{1}{2}(\text{LSE}_{10} + \text{LSE}_{11})$; $\Delta\varepsilon$ is the difference in LSE of two bands, calculated as $\Delta\text{LSE} = \text{LSE}_{10} - \text{LSE}_{11}$; $c_0, c_1, \ldots, c_6$ are algorithm coefficients derived from atmospheric simulation codes; w is the total atmospheric water vapor content in $\text{g}\,\text{cm}^{-2}$ unit. For Landsat 8 TIR bands 10 and 11, Equation (13) can be rewritten as

$$\begin{aligned}\text{LST} = T_{\text{ToA}\,10} + c_0 + c_1\left(T_{\text{ToA}\,10} - T_{\text{ToA}\,11}\right) + c_2\left(T_{\text{ToA}\,10} - T_{\text{ToA}\,11}\right)^2 \\ + \left(c_3 + c_4 w\right)\left(1 - \text{LSE}_\text{mean}\right) + \left(c_5 + c_6 w\right)\Delta\text{LSE}. \end{aligned}\tag{14}$$

The coefficients $(c_0, c_1, \ldots, c_6)$ for this algorithm, specifically for Landsat 8 data, are given by Jiménez-Muñoz et al. [37]. They have used the GAPRI database to estimate the coefficients using MODTRAN simulation codes. Further details regarding GAPRI database can be found in [37]; determination procedure for algorithm coefficients from different atmospheric databases can be found in [42,58].

The seven coefficient values for Jiménez-Muñoz et al.'s Split-Window algorithm are presented in Table 3. The atmospheric water vapor content (w) is not included during the determination of coefficients; it has to be put in the mathematical Expression (14) of the algorithm directly.

Table 3. Split-Window Algorithm coefficients for Jiménez-Muñoz et al.'s (2014) algorithm as obtained from numerical simulation. Source: Reference [37]. RMSE = Root-mean-squared-error.

Coefficient	Value	RMSE
c_0	−0.268	
c_1	1.378	
c_2	0.183	
c_3	54.30	0.984
c_4	−2.238	
c_5	−129.20	
c_6	16.40	

3.4. Split-Window Algorithm by Du et al. (2015) with Coefficients

The Split-Window Algorithm for Landsat 8 data proposed by Du et al. (2015) [40] is based on the generalized Split-Window algorithm by Wan [39], which was developed for MODerate Resolution Imaging Spectrometer (MODIS) data. The Du et al. algorithm was developed specifically for Landsat 8 data; they named this method as practical Split-Window Algorithm. The mathematical expression of the algorithm is [40]:

$$\text{LST} = b_0 + \left(b_1 + b_2\frac{1-\varepsilon_\text{m}}{\varepsilon_\text{m}} + b_3\frac{\Delta\varepsilon}{\varepsilon^2}\right)\frac{T_i + T_j}{2} + \left(b_4 + b_5\frac{1-\varepsilon_\text{m}}{\varepsilon_\text{m}} + b_6\frac{\Delta\varepsilon}{\varepsilon^2}\right)\frac{T_i - T_j}{2} + b_7\left(T_i - T_j\right)^2. \tag{15}$$

where $b_0, b_1, \ldots b_7$ are algorithm coefficients derived from atmospheric profile dataset using simulation codes. All other parameters in Equation (15) are same as in Equation (13), except the w in Equation (13), which is absent in Equation (15).

Equation (15) for Landsat 8 data, with more specific expressions, can be rewritten as

$$\begin{aligned}\text{LST} = b_0 + \left(b_1 + b_2\frac{1 - \text{LSE}_\text{mean}}{\text{LSE}_\text{mean}} + b_3\frac{\Delta\text{LSE}}{(\text{LSE})^2}\right)\frac{T_{\text{ToA}\,10} + T_{\text{ToA}\,11}}{2} \\ + \left(b_4 + b_5\frac{1 - \text{LSE}_\text{mean}}{\text{LSE}_\text{mean}} + b_6\frac{\Delta\text{LSE}}{(\text{LSE})^2}\right)\frac{T_{\text{ToA}\,10} - T_{\text{ToA}\,11}}{2} + b_7\left(T_{\text{ToA}\,10} - T_{\text{ToA}\,11}\right)^2. \end{aligned}\tag{16}$$

Other than the algorithm coefficients, parameters in this equation are same as in Equation (14). The coefficients ($b_0, b_1, \ldots b_7$) for this algorithm were estimated by Du et al. [40] under different atmospheric and surface conditions, through numerical simulation, and using atmospheric profiles. As atmospheric profile they have used the TIGR database; and to perform the numerical simulation they used the MODTRAN 5.2 atmospheric transmittance/radiance codes. They used water vapor content (w) divided into five sub-ranges to calculate the coefficients. Under different atmospheric conditions, users can use the coefficients for their needed sub-ranges. Further details regarding the procedure of algorithm coefficients' estimation can be found in [40]. The coefficients for Du et al. algorithm covering different w sub-ranges are presented in Table 4.

Table 4. Split-Window Algorithm coefficients for Du et al.'s (2015) method as estimated from numerical simulation. Source: Reference [40].

w (g cm^{-2})	b_0	b_1	b_2	b_3	b_4	b_5	b_6	b_7	RMSE (K)
[0.0, 2.5]	−2.78009	1.01408	0.15833	−0.34991	4.04487	3.55414	−8.88394	0.09152	0.34
[2.0, 3.5]	11.00824	0.95995	0.17243	−0.28852	7.11492	0.42684	−6.62025	−0.06381	0.60
[3.0, 4.5]	9.62610	0.96202	0.13834	−0.17262	7.87883	5.17910	−13.26611	−0.07603	0.71
[4.0, 5.5]	0.61258	0.99124	0.10051	−0.09664	7.85758	6.86626	−15.00742	−0.01185	0.86
[5.0, 6.3]	−0.34808	0.98123	0.05599	−0.03518	11.96444	9.06710	−14.74085	−0.20471	0.93
[0.0, 6.3]	−0.41165	1.00522	0.14543	−0.27297	4.06655	−6.92512	−18.27461	0.24468	0.87

Using the two Split-Window LST retrieval algorithms in Equations (14) and (16), along with their respective coefficients, LST can be determined once the column water vapor (w) of the study area, ToA brightness temperature (T_{ToA}) for both thermal bands, and LSE information is available. The T_{ToA} is usually estimated from the thermal bands of remote sensing data while the LSE is determined using optical bands as described in the following sections.

3.5. Normalized Difference Vegetation Index and the Proportion of Vegetation Cover

In scientific studies of land resources, vegetation index is often used to express the amount of living plant coverage on lands. The term to mathematically express this indication is called Normalized Difference Vegetation Index, or NDVI for short. It is calculated from the visible red and near-infrared (NIR) light reflected by vegetation and can be expressed as

$$\text{NDVI}_{\text{DN}} = \frac{\text{NIR} - \text{Red}}{\text{NIR} + \text{Red}}, \tag{17}$$

where the subscript "DN" stands for "Digital Number"; it implies that the calculation was made using level-1 DN values stored in remote sensing images. As remote sensing images are subject to cloud covers, atmospheric scattering effects, viewing angle problem, etc., the raw RS data need to be converted into surface reflectance values correcting those effects. In practice, the level-1 DN values are first converted into top-of-atmosphere (ToA) spectral reflectance ($\rho_{\lambda,\text{ToA}}$). It is a unitless quantity and can be calculated from OLI data of Landsat 8 as [48]:

$$\rho_{\lambda,\text{ToA}(\theta)} = M_\rho \times Q_{\text{cal}} + A_\rho, \tag{18}$$

where M_ρ is the reflectance multiplicative scaling factor for the given band, available in the image metadata file as `REFLECTANCE_MULT_BAND_`n, with n being 1 through 9; A_ρ is the reflectance additive scaling factor for the given band, available in the same file as `REFLECTANCE_ADD_BAND_`n, with n being 1 through 9; Q_{cal} is the level-1 pixel value stored as DN values in the image for both OLI and TIR bands; the θ on left hand side means that this reflectance ($\rho_{\lambda,\text{ToA}(\theta)}$) does not involve the correction for sun elevation angle.

Making the correction for sun elevation angle, we can exclude the θ from reflectance notation and express the reflectance as [48]:

$$\rho_{\lambda,\text{ToA}} = \frac{\rho_{\lambda,\text{ToA}(\theta)}}{\sin\theta}, \tag{19}$$

where $\rho_{\lambda,\text{ToA}(\theta)}$ is the ToA spectral reflectance without sun elevation angle correction as calculated in Equation (18); θ is solar elevation angle, which is the local sun elevation angle at the time of satellite overpass available in the image metadata file of Landsat 8 as SUN_ELEVATION. This value needs to be checked for each Landsat 8 scene. The sun elevation angle can be related with solar zenith angle (θ_z) using cosine function as

$$\rho_{\lambda,\text{ToA}} = \frac{\rho_{\lambda,\text{ToA}(\theta)}}{\cos(\theta_z)}, \tag{20}$$

where θ_z is the solar zenith angle with $\theta_z = 90° - \theta$. Combining Equations (18) and (19), we can calculate ToA spectral reflectance as

$$\rho_{\lambda,\text{ToA}} = \frac{M_\rho \times Q_{\text{cal}} + A_\rho}{\sin\theta}. \tag{21}$$

To determine NDVI, we need the reflectance values for red and near-infrared bands; this translates to band 4 and band 5 of Landsat 8 image, respectively. The red band in Landsat 8 covers 0.636 to 0.673 µm and NIR band 0.851 to 0.879 µm in the electromagnetic spectrum [48]. For band 4 and band 5, M_ρ value is 2.0000×10^{-5}, and A_ρ value is -0.100000 [48], as given in the image metadata file.

Once the reflectance is corrected for the sun elevation angle, it needs another correction—the atmospheric correction because the ToA spectral reflectance includes atmospheric scattering effects and therefore does not represent the true reflectance of land surfaces. In order to get the reflectance from the surface ($\rho_{\lambda,\text{LS}}$), we need to correct atmospheric effects including the cloud cover and atmospheric gases. This correction can be made using some atmospheric correction modules available in various image processing software. Then, surface reflectance can be determined using Equation (21).

To simplify the notation of surface reflectance, in the following we used ρ in place of $\rho_{\lambda,\text{LS}}$. According to this notation, the NDVI of land surface (NDVI$_{\text{LS}}$) can be expressed as

$$\text{NDVI}_{\text{LS}} = \frac{\rho_{\text{NIR}} - \rho_{\text{red}}}{\rho_{\text{NIR}} + \rho_{\text{red}}}. \tag{22}$$

For Landsat 8 image data, Equation (22) takes the form:

$$\text{NDVI}_{\text{LS}} = \frac{\rho_{\text{band 5}} - \rho_{\text{band 4}}}{\rho_{\text{band 5}} + \rho_{\text{band 4}}}. \tag{23}$$

Using NDVI$_{\text{LS}}$ values as in Equation (23), the proportion of vegetation cover can be calculated as [64]:

$$P_{\text{v}} = \left(\frac{\text{NDVI}_{\text{LS}} - \text{NDVI}_{\text{min}}}{\text{NDVI}_{\text{max}} - \text{NDVI}_{\text{min}}} \right)^2, \tag{24}$$

where NDVI$_{\text{max}} = 0.5$ indicates the presence of vegetation on lands, and NDVI$_{\text{min}} = 0.2$ represents only bare soil on land surfaces. NDVI value less than 0 indicates the water, and NDVI value greater than 0.5 indicates full vegetation [65]. When NDVI value ranges between 0.2 and 0.5, the surface is considered as a mixture of soil and vegetation, requiring the calculation of P_{v} using Equation (24). Using the P_{v}, the emissivity of the mixed land surface is then estimated as described in the following Section.

3.6. Land Surface Emissivity Determination

Quantitatively, emissivity is the ratio of the thermal radiation from a surface to the radiation from an ideal black surface at the same temperature as given by the Stefan–Boltzmann law [1]. To retrieve

LST from ToA brightness temperature (see Section 3.7), we must consider emissivity from land surfaces. The term Land Surface Emissivity (LSE) is used to indicate emissivity from land surfaces that are composed of different types of materials (soils, vegetation, water etc.). One way to get LSE is through normalized difference vegetation index since NDVI represents the greenness of land surfaces, giving an idea of types of materials comprising the land surfaces. Thus, different values of NDVI represent different materials of land surfaces. If the NDVI value is less than 0.2, then it represents only bare soil. In this case, the emissivity can be calculated from reflectivity values in red region of the image. If the NDVI value is greater than 0.5, then the land surface is composed of vegetation only. If that is the case in a real study, a constant value of emissivity, typically 0.99, can be used [21]. But in situations when NDVI lies between 0.2 and 0.5, LSE for a given band *i* can be related with NDVI and proportion of vegetation (P_v) as [41]:

$$\text{LSE}_i = \begin{cases} a_i \rho_{\text{red}} + b_i & \text{NDVI} < 0.2 \\ \varepsilon_{v,i} P_v + \varepsilon_{s,i}(1 - P_v) + C_i & 0.2 \leq \text{NDVI} \leq 0.5 \\ \varepsilon_{v,i} + C_i & \text{NDVI} > 0.5, \end{cases} \tag{25}$$

where $\varepsilon_{v,i}$ is the emissivity of fully vegetated surfaces and $\varepsilon_{s,i}$ is emissivity of barren soil, in the band *i*; P_v is the proportion of vegetation as calculated in Equation (24); a_i, b_i are the coefficients that can be estimated from laboratory spectra of soils using statistical fits, assuming that the emissivity and the reflectivities in red band have a linear relationship [66]. The symbol C_i in the above equation denotes the roughness of land surfaces [65]. For plain and homogeneous land surfaces, this C_i can be neglected [21], and considered $C_i = 0$ [65]. For rough and heterogeneous surfaces, i.e., soil-vegetation mixed pixels, C_i denotes the increment in emissivity resulted from the cavity effect and multiple scattering in the mixed pixels [67].

Taking emissivity values of soil and vegetation into account, and assuming that NDVI values of earth surfaces range from around 0.2 to 0.5, the emissivity of land surfaces (LSE) can be calculated according to the NDVI-threshold method as [41,66]:

$$\text{LSE} = \varepsilon_v P_v + \varepsilon_s (1 - P_v) + C. \tag{26}$$

The *C* in the above equation is the same as in Equation (25), which can be found also as *dε* in literature [21].

According to Equation (26), to calculate LSE for Landsat 8 thermal bands, we need the ε_s and ε_v values estimated for both TIR bands. Yu et al. [41] estimated these values using the MODIS UCSB (University of California, Santa Barbara, CA, USA) emissivity library (https://icess.eri.ucsb.edu/modis/EMIS/html/em.html), as presented in Table 5.

Table 5. Emissivity values of soil and vegetation for TIR band 10 and band 11. Source: Reference [41].

	Emissivity Values	
TIR Band	**Vegetation (ε_v)**	**Soil (ε_s)**
band 10	0.9863	0.9668
band 11	0.9896	0.9747

In Equation (26), an approximation of *C* is given by [41,68]:

$$C = (1 - \varepsilon_s)(1 - P_v) F \varepsilon_v, \tag{27}$$

where *F* is a shape factor [69]. Sobrino et al. [21] considered this shape factor (*F*) under different geometrical distributions having a mean value of 0.55.

Taking Equations (26) and (27) into account, the LSE can be calculated as

$$\text{LSE} = m\, P_\text{v} + n, \tag{28}$$

with

$$m = \varepsilon_\text{v} - \varepsilon_\text{s} - (1 - \varepsilon_\text{s})\, F\varepsilon_\text{v} \quad \text{and} \quad n = \varepsilon_\text{s} + (1 - \varepsilon_\text{s})\, F\varepsilon_\text{v}.$$

Based on the emissivity values in Table 5 and the mathematical expression in Equation (28), the LSE for both TIR bands of Landsat 8 data can be calculated. To do so, we first need to calculate the m and n values for these bands. For TIR band 10, we get

$$m_\text{TIR 10} = 0.9863 - 0.9668 - (1 - 0.9668) \times 0.55 \times 0.9863 \approx 0.0015,$$
$$n_\text{TIR 10} = 0.9668 + (1 - 0.9668) \times 0.55 \times 0.9863 \approx 0.9848.$$

Thus, using Equation (28), we get the LSE for TIR band 10 as

$$\text{LSE}_\text{TIR 10} = 0.0015\, P_\text{v} + 0.9848. \tag{29}$$

Similarly, for TIR band 11, we get

$$m_\text{TIR 11} = 0.9896 - 0.9747 - (1 - 0.9747) \times 0.55 \times 0.9896 \approx 0.0011,$$
$$n_\text{TIR 11} = 0.9747 + (1 - 0.9747) \times 0.55 \times 0.9896 \approx 0.9885.$$

Therefore, LSE for TIR band 11 can be expressed as

$$\text{LSE}_\text{TIR 11} = 0.0011\, P_\text{v} + 0.9885. \tag{30}$$

Using the proportion of vegetation cover as described in Section 3.5 and expressed in Equation (24), LSE for TIR band 10 and band 11 can be calculated using Equations (29) and (30), respectively.

3.7. Top-of-Atmosphere (ToA) Brightness Temperature Determination

Determination of ToA brightness temperature (T_ToA) can be described as a two-step process. The first step includes the conversion of level-1 DN values of Landsat 8 thermal infrared data to at-satellite (or at-sensor, or ToA) spectral radiance values. This is the spectral radiance in wavelength of a surface, which is expressed with $L_{\lambda,\text{ToA}}$ and has a unit of watt per meter squared per steradian per micro meter ($\text{W}\,\text{m}^{-2}\,\text{sr}^{-1}\,\text{µm}^{-1}$). The formula to convert level-1 DN values in RS images to spectral radiance is [48]:

$$L_{\lambda,\text{ToA}} = M_L \times Q_\text{cal} + A_L, \tag{31}$$

where M_L is the radiance multiplicative scaling factor for the given band, available in the image metadata file as `RADIANCE_MULT_BAND_n`, with n being 1 through 11; A_L is the radiance additive scaling factor for the given band, available in the same file as `RADIANCE_ADD_BAND_n`, with n being 1 through 11; Q_cal is the level-1 pixel value stored as DN values in the image, available for both OLI and TIRS bands. The M_L value for both TIR bands (band 10 and band 11) is 3.3420×10^{-4}; and A_L value for both of these bands is 0.10000. Spectral radiance can be obtained for both OLI and TIR bands but in order to retrieve LST from Landsat 8 thermal bands, radiance from only thermal bands is necessary. For both TIR bands, $L_{\text{ToA 10}}$ and $L_{\text{ToA 11}}$ can be estimated following Equation (31).

The second step to determine T_ToA involves the use of $L_{\lambda,\text{ToA}}$ image data from Equation (31). Then, T_ToA in K (Kelvin) unit can be calculated by inverting Planck's radiation equation as [48]:

$$T_\text{ToA} = \frac{K_2}{\ln\left(\frac{K_1}{L_{\lambda,\text{ToA}}} + 1\right)}, \tag{32}$$

where K_1 and K_2 are the thermal conversion constants for the given band, available in the image metadata file as `K1_CONSTANT_BAND_`n and `K2_CONSTANT_BAND_`n, respectively, with n being 10 or 11; $L_{\lambda,\text{ToA}}$ is the ToA spectral radiance calculated for band 10 or band 11 with Equation (31). The K_1 and K_2 are numerical constant values for TIR bands of Landsat 8; for band 10 the values are 774.8853 and 1321.0789, respectively; for band 11 they are 480.8883 and 1201.1442, respectively.

The ToA brightness temperature in °C (degree Celsius) unit can be estimated by subtracting 273.15 in Equation (32) as

$$T_{\text{ToA}} = \frac{K_2}{\ln\left(\frac{K_1}{L_{\lambda,\text{ToA}}} + 1\right)} - 273.15. \tag{33}$$

According to Equation (33), the $T_{\text{ToA 10}}$ and $T_{\text{ToA 11}}$ for both TIR bands of Landsat 8 can be estimated in °C unit.

3.8. Preparation and Processing of Data for LST Retrieval from Landsat 8

In order to perform atmospheric corrections of Landsat 8 data, as well as for other processing of raster images, different computer tools were used in this study. First, appropriate Landsat 8 images were downloaded from the website of USGS earth explorer. Vector shapefiles were downloaded from the GADM website (http://gadm.org/data.html). Spatial subset of the raster image was created using the shapefile for our study area in QGIS [70] software. Atmospheric corrections including the removal of cloud and haze from the level-1 Landsat 8 data were done using the ATCOR module in PCI Geomatica 2016 software. From the atmospherically corrected subset image data, NDVI was determined using raster calculator of QGIS. Other calculations, for example, proportion of vegetation cover, LSE, LST, etc. were also estimated with the same tool. The LST maps were exported using the print composer function of QGIS. Statistical analyses and all types of plots and histograms were created using the R program [71] with substantial help from the `raster` [72], `rgdal` [73], `ggplot2` [74], and `caret` [75] libraries.

4. Results and Discussion

The LST products retrieved from all four algorithms were validated against reference LST (LST$_{\text{ref}}$) and cross-validated against MODIS daily LST (LST$_{\text{MOD}}$). The RMSE (root-mean-squared-error) was used to measure the accuracy of LST retrieved with four methods comparing them against reference LST and MODIS LST. The reference LSTs for all Landsat 8 images were estimated using the ATCOR module available in PCI Geomatica 2016 software. The MODIS daily LST was retrieved using the A$\rho\rho$EEARS online application from the Terra MODIS images. The online atmospheric correction calculator (https://atmcorr.gsfc.nasa.gov/) was used for the estimation of atmospheric parameters, including the water vapor content. For several locations in the study area, a total of 48 calculations of w for each Landsat 8 scene were made using the online tool and the w range was found to be 0.6 to 3.0 g cm^{-2} considering all five Landsat 8 images. Therefore, we have used several values of w for LST retrieval.

The LST result retrieved with the RTE-based direct method is denoted as LST$_{\text{RTE}}$, LST with Single-Channel algorithm as LST$_{\text{SC}}$, and LSTs with two Split-Window algorithms as LST$_{\text{Jim}}$ (for Jiménez-Muñoz et al.'s method), and LST$_{\text{Du}}$ (for Du et al.'s method). In the following, the LST results from all four algorithms for the Landsat 8 image of 21 February 2018 (Sections 4.1–4.4) are presented along with an intercomparison study among them (Section 4.5). In addition, variation in LST results with varied amount of w is discussed in Section 4.6. Intercomparison results from the cross-validation of Landsat 8 LSTs against MODIS daily LSTs are presented in Section 4.7.

4.1. Results from RTE Method using TIR Band 10

The atmospheric parameters required to retrieve LST in direct method using RTE (3) were obtained using the online atmospheric correction calculator for six specific locations of the study area as presented in Table 6. The values in several observations were found to be close to each other.

In order to compute the RMSE, we first calculated ΔLST comparing the RTE-retrieved LST and the reference LST. The validation results are represented with histograms in Figure 4 including the RMSE values. The smallest RMSE for LST_{RTE} was found to be 1.95 °C, with the largest being 2.67 °C.

Table 6. Atmospheric parameters retrieved through online atmospheric correction calculator for the Landsat 8 image of 21 February 2018 (L_{up} and L_{down} are in $W\,m^{-2}\,sr^{-1}\,\mu m^{-1}$ unit).

Location		Atmospheric Parameters			
Latitude	Longitude	τ	L_{up}	L_{down}	w (g cm^{-2})
23°20′ N	91°0′ E	0.76	1.97	3.23	1.87–2.32
23°20′ N	91°22′ E	0.78	1.85	3.04	1.68–2.32
23°27′ N	90°57′ E	0.77	1.91	3.14	1.87–2.43
23°24′ N	90°55′ E	0.77	1.92	3.16	1.87–2.43
23°28′ N	91°0′ E	0.76	1.94	3.19	1.87–2.32
23°21′ N	90°56′ E	0.77	1.93	3.17	1.87–2.41
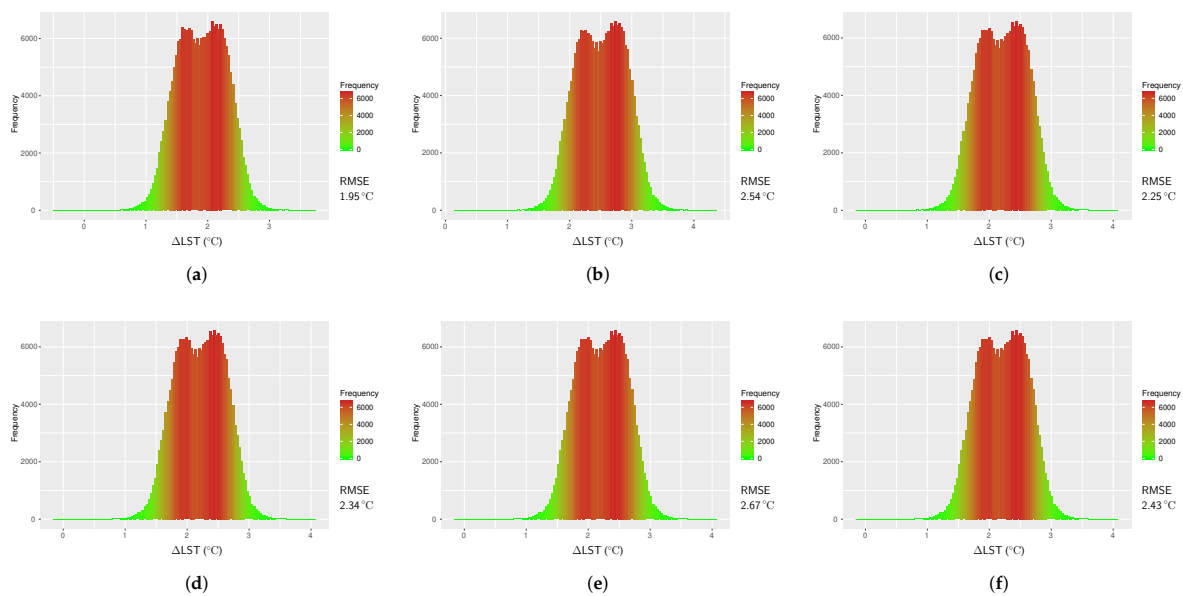
Figure 4. Histograms of temperature difference between the reference LST (LST_{ref}) and LST from Radiative Transfer Equation (RTE)-based algorithm (LST_{RTE}) for Landsat 8 image of 21 February 2018; (**a**) $\tau = 0.76$, $L_{up} = 1.97$, $L_{down} = 3.23$, (**b**) $\tau = 0.78$, $L_{up} = 1.85$, $L_{down} = 3.04$, (**c**) $\tau = 0.77$, $L_{up} = 1.91$, $L_{down} = 3.14$, (**d**) $\tau = 0.77$, $L_{up} = 1.92$, $L_{down} = 3.16$, (**e**) $\tau = 0.76$, $L_{up} = 1.94$, $L_{down} = 3.19$, and (**f**) $\tau = 0.77$, $L_{up} = 1.93$, $L_{down} = 3.17$ (L_{up} and L_{down} are in $W\,m^{-2}\,sr^{-1}\,\mu m^{-1}$ unit).

### 4.2. Results from Single-Channel Algorithm using TIR Band 10

The LST retrieved with Single-Channel algorithm from band 10 of Landsat 8 uses Equation (4) and atmospheric functions calculated for different values of water vapor content as given in Table 2. For our study area, we retrieved LSTs for w range of 0.5 to 3.0 g cm^{-2} with an interval of 0.5 g cm^{-2}. This gives LST calculations for six values of w. All LST products obtained in this method were then validated against reference LST as shown in Figure 5 with their RMSEs. The smallest RMSE was found to be 4.16 °C for $w = 3.0$ g cm^{-2}, whereas the largest RMSE was 4.17 °C for $w = 0.5$ g cm^{-2}.
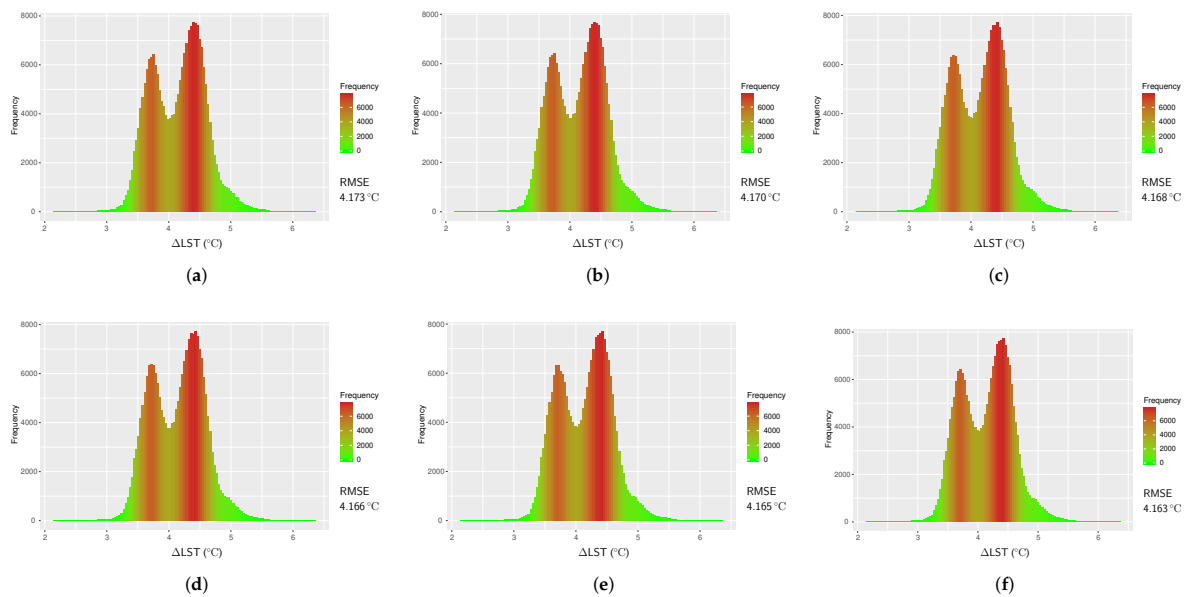
Figure 5. Histograms of temperature difference between the reference LST (LST$_{ref}$) and LST from Single-Channel algorithm (LST$_{SC}$) for Landsat 8 image of 21 February 2018; (**a**) $w = 0.5\,\mathrm{g\,cm^{-2}}$, (**b**) $w = 1.0\,\mathrm{g\,cm^{-2}}$, (**c**) $w = 1.5\,\mathrm{g\,cm^{-2}}$, (**d**) $w = 2.0\,\mathrm{g\,cm^{-2}}$, (**e**) $w = 2.5\,\mathrm{g\,cm^{-2}}$, and (**f**) $w = 3.0\,\mathrm{g\,cm^{-2}}$.

4.3. Results from Jiménez-Muñoz et al.'s Split-Window Algorithm

The coefficient values in Jiménez-Muñoz et al.'s (2014) algorithm (see Table 3) do not include the water vapor content (w); instead, the algorithm in Equation (14) takes the w as a direct input from the user. Like in Single-Channel algorithm, we used six values of w to retrieve LSTs in this method (LST$_{Jim}$). To compute RMSEs, all observations of LST$_{Jim}$ were validated against reference LST and presented as histograms in Figure 6. The smallest RMSE for LST$_{Jim}$ was found to be 0.74 °C when $w = 0.5\,\mathrm{g\,cm^{-2}}$, with the largest RMSE being 0.94 °C when $w = 3.0\,\mathrm{g\,cm^{-2}}$.
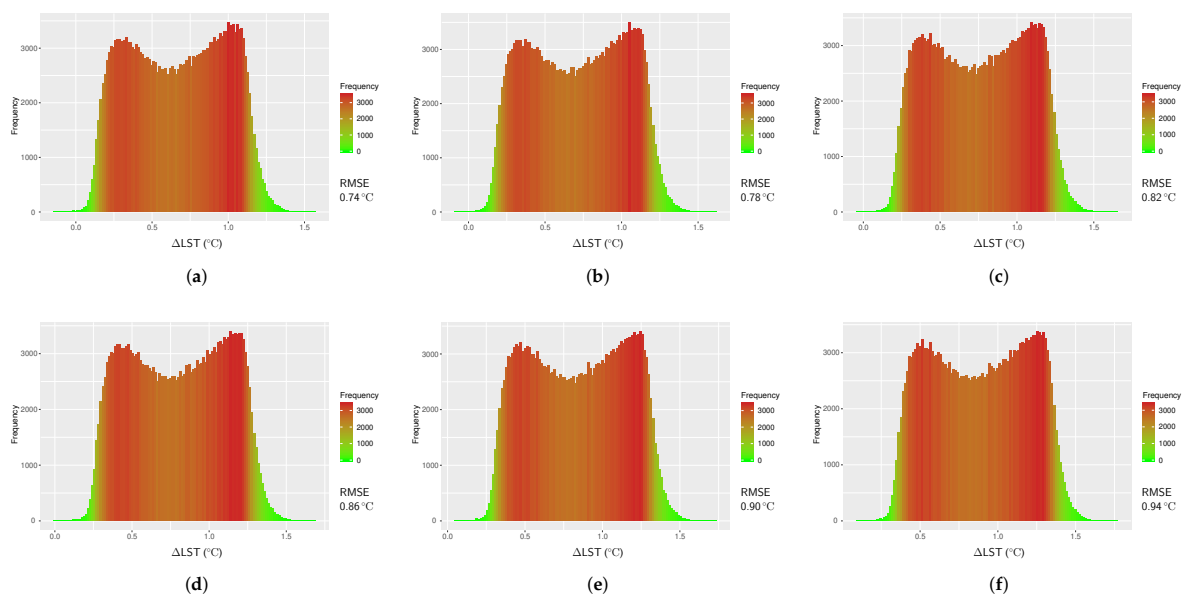
Figure 6. Histograms of temperature difference between the reference LST (LST$_{ref}$) and LST from Jiménez-Muñoz et al.'s Split-Window algorithm (LST$_{Jim}$) for Landsat 8 image of 21 February 2018; (**a**) $w = 0.5\,\mathrm{g\,cm^{-2}}$, (**b**) $w = 1.0\,\mathrm{g\,cm^{-2}}$, (**c**) $w = 1.5\,\mathrm{g\,cm^{-2}}$, (**d**) $w = 2.0\,\mathrm{g\,cm^{-2}}$, (**e**) $w = 2.5\,\mathrm{g\,cm^{-2}}$, and (**f**) $w = 3.0\,\mathrm{g\,cm^{-2}}$.

4.4. Results from Du et al.'s Split-Window Algorithm

As it is mentioned previously, the coefficient values in Du et al.'s (2015) algorithm were estimated using water vapor contents (w) of various sub-ranges (see Table 4). Therefore, LSTs were estimated with this algorithm (LST$_{\text{Du}}$) using algorithm coefficients given for w sub-ranges of 0.0 to 2.5 g cm^{-2}, 2.0 to 3.5 g cm^{-2}, 3.0 to 4.5 g cm^{-2}, 4.0 to 5.5 g cm^{-2}, 5.0 to 6.3 g cm^{-2}, and 0.0 to 6.3 g cm^{-2}. All six LSTs were then validated against reference LST and RMSEs were computed (Figure 7). The smallest RMSE (1.13 °C) was found when LST was estimated using w in 0.0 to 6.3 g cm^{-2} while in w range of 2.0 to 3.5 g cm^{-2} the LST was found with abnormally the largest RMSE (11.05 °C). This error could be due to the wrong use of w amount (see Section 4.6).
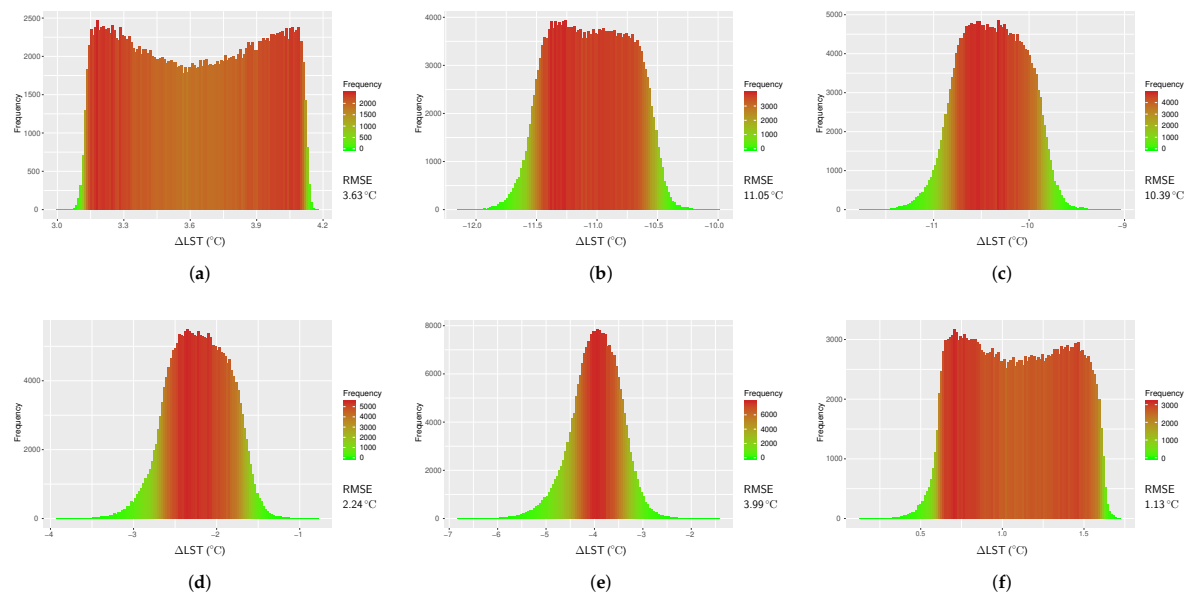
Figure 7. Histograms of temperature difference between the reference LST (LST$_{\text{ref}}$) and LST from Du et al.'s Split-Window algorithm (LST$_{\text{Du}}$) for Landsat 8 image of 21 February 2018; (**a**) $w = 0.0$ to 2.5 g cm^{-2}, (**b**) $w = 2.0$ to 3.5 g cm^{-2}, (**c**) $w = 3.0$ to 4.5 g cm^{-2}, (**d**) $w = 4.0$ to 5.5 g cm^{-2}, (**e**) $w = 5.0$ to 6.3 g cm^{-2}, and (**f**) $w = 0.0$ to 6.3 g cm^{-2}.

4.5. Intercomparison of Four Algorithms to Retrieve LST from Landsat 8 Against Reference LSTs

The LST results as estimated from the Landsat 8 image of 21 February 2018 with all four algorithms (see Sections 4.1–4.4) were compared among them validating the results against reference LST by means of RMSE computation and R^2 (coefficient of determination). In addition, algorithm-retrieved LSTs were also observed against reference LST by means of mean bias error (Bias$_{\text{ref}}$).

Except for LST$_{\text{RTE}}$, a sub-range of w was considered for the average LST values for three other methods (LST$_{\text{SC}}$, LST$_{\text{Jim}}$, and LST$_{\text{Du}}$). Considering the water vapor content of 1.68 to 2.43 g cm^{-2} for the 21 February 2018 Landsat 8 image, as retrieved from the NCEP database with MODTRAN codes, a w range of 1.5 to 3.0 g cm^{-2} was considered as the possible mean of w for LST$_{\text{SC}}$ and LST$_{\text{Jim}}$ methods. For the LST$_{\text{Du}}$ method, the algorithm coefficients available in w range of 0.0 to 6.3 g cm^{-2}, that is, the entire range of w was considered.

The minimum and maximum LST, along with the statistical mean and standard deviation of LST retrieved with four methods, and the reference LST are presented in Table 7. The RMSE and R^2, as well as the mean bias (Bias$_{\text{ref}}$) of algorithm-retrieved LSTs computed against reference LST, are also presented.

Table 7. Intercomparison results of LSTs retrieved with four algorithms from Landsat 8 data (21 February 2018) against reference LSTs.

| LST Method | w (g cm^{-2}) | LST Estimates (°C) | | | | Comparison Results | | |
		MIN	MAX	MEAN	SD	RMSE (°C)	R^2	Bias $_{ref}$ (°C)
LST$_{ref}$	–	25.00	34.00	27.80	0.8237	–	–	–
LST$_{RTE(avg)}$	1.68–2.43	24.00	31.33	25.50	0.7081	2.20	0.77	2.30
LST$_{SC}$	0.5	22.38	28.13	23.65	0.5542	4.17	0.76	4.15
	1.0	22.38	28.14	23.65	0.5545	4.17	0.76	4.15
	1.5	22.38	28.14	23.66	0.5548	4.17	0.76	4.15
	2.0	22.38	28.15	23.66	0.5552	4.17	0.76	4.14
	2.5	22.38	28.15	23.66	0.5557	4.16	0.76	4.14
	3.0	22.38	28.16	23.66	0.5562	4.16	0.76	4.14
	3.5	22.38	28.17	23.66	0.5568	4.16	0.76	4.14
	4.0	22.38	28.18	23.66	0.5575	4.16	0.76	4.14
	4.5	22.38	28.19	23.67	0.5583	4.16	0.76	4.14
LST$_{SC(avg)}$	1.5–3.0	22.38	28.15	23.66	0.5555	4.17	0.76	4.14
LST$_{Jim}$	0.5	24.99	32.83	27.13	0.7106	0.74	0.86	0.67
	1.0	24.94	32.75	27.09	0.7103	0.78	0.86	0.71
	1.5	24.93	32.63	27.04	0.7101	0.82	0.86	0.76
	2.0	24.87	32.70	27.00	0.7098	0.86	0.86	0.80
	2.5	24.83	32.65	26.96	0.7095	0.90	0.86	0.84
	3.0	24.80	32.61	26.92	0.7093	0.94	0.86	0.88
	3.5	24.76	32.57	26.87	0.7090	0.93	0.86	0.93
	4.0	24.73	32.52	26.83	0.7088	1.02	0.86	0.97
	4.5	24.69	32.48	26.79	0.7085	1.06	0.86	1.01
LST$_{Jim(avg)}$	1.5–3.0	24.86	32.65	26.98	0.7097	0.88	0.86	0.82
LST$_{Du}$	0.0–2.5	21.94	30.24	24.18	0.7514	3.63	0.87	3.62
	2.0–3.5	35.97	45.41	38.85	0.8432	11.05	0.86	−11.05
	3.0–4.5	35.06	45.06	38.18	0.8929	10.39	0.85	−10.38
	4.0–5.5	26.75	37.23	30.01	0.9350	2.24	0.85	−2.21
	5.0–6.3	27.51	39.98	31.76	1.1160	3.99	0.82	−3.96
	0.0–6.3	24.23	33.23	26.72	0.8070	1.13	0.86	1.08

As seen in Table 7, the mean RMSE was found 2.20 °C for LST$_{RTE}$; 4.17 °C for LST$_{SC}$; 0.88 °C for LST$_{Jim}$; and 1.13 °C for LST$_{Du}$. The average correlation of coefficient (R^2) for LST$_{Jim}$ and LST$_{Du}$ is 0.86; it is 0.77 for LST$_{RTE}$, and 0.76 for LST$_{SC}$ method. This indication implies that all four algorithms perform efficiently compared to reference LST. The mean bias against reference LST (bias$_{ref}$) is the smallest in LST$_{Jim}$ (0.82 °C) and largest in LST$_{SC}$ (4.14 °C), with LST$_{Du}$ (1.08 °C) and LST$_{RTE}$ (2.30 °C) being in between. Considering all these observations, the best performing LST algorithm in our study is LST$_{Jim}$, with the other three methods staying in close agreement.

The box plots in Figure 8 represent LST results of four algorithms in terms of RMSE, giving a visual aid for intercomparison. As seen in this figure, variation in RMSE is lowest for LST$_{Jim}$, with LST$_{RTE}$ and LST$_{SC}$ being next to it and LST$_{Du}$ having the highest variation. The rather different RMSE variation in LST$_{Du}$ is probably due to the wrong use of w, which is described in Section 4.6.

The LST maps created using all four methods and with ATCOR module (LST$_{ref}$) are shown in Figure 9. We presented the maps with LST results that were found very close to the reference LST, considering the possible amount of w present in our study area. This makes the LST maps for LST$_{SC}$ and LST$_{Jim}$ computed with $w = 2.0$ g cm^{-2}, and LST$_{Du}$ computed with w range of 0.0 to 6.3 g cm^{-2}.
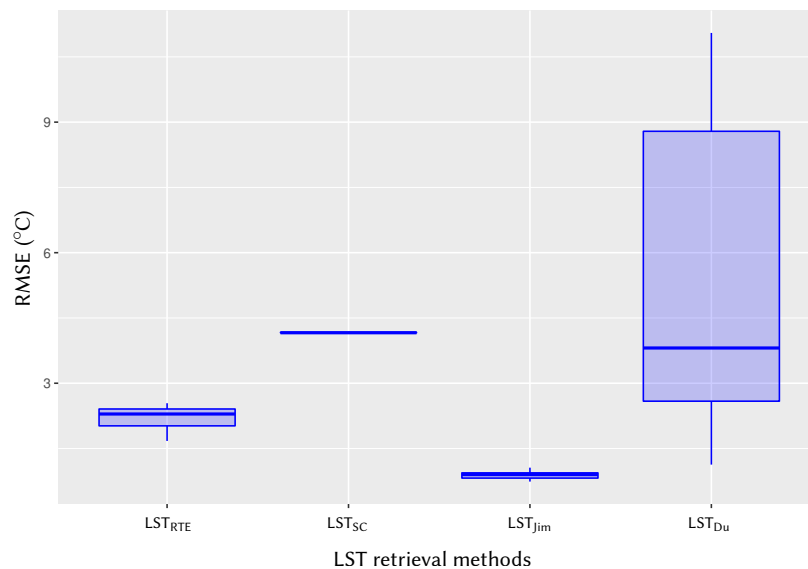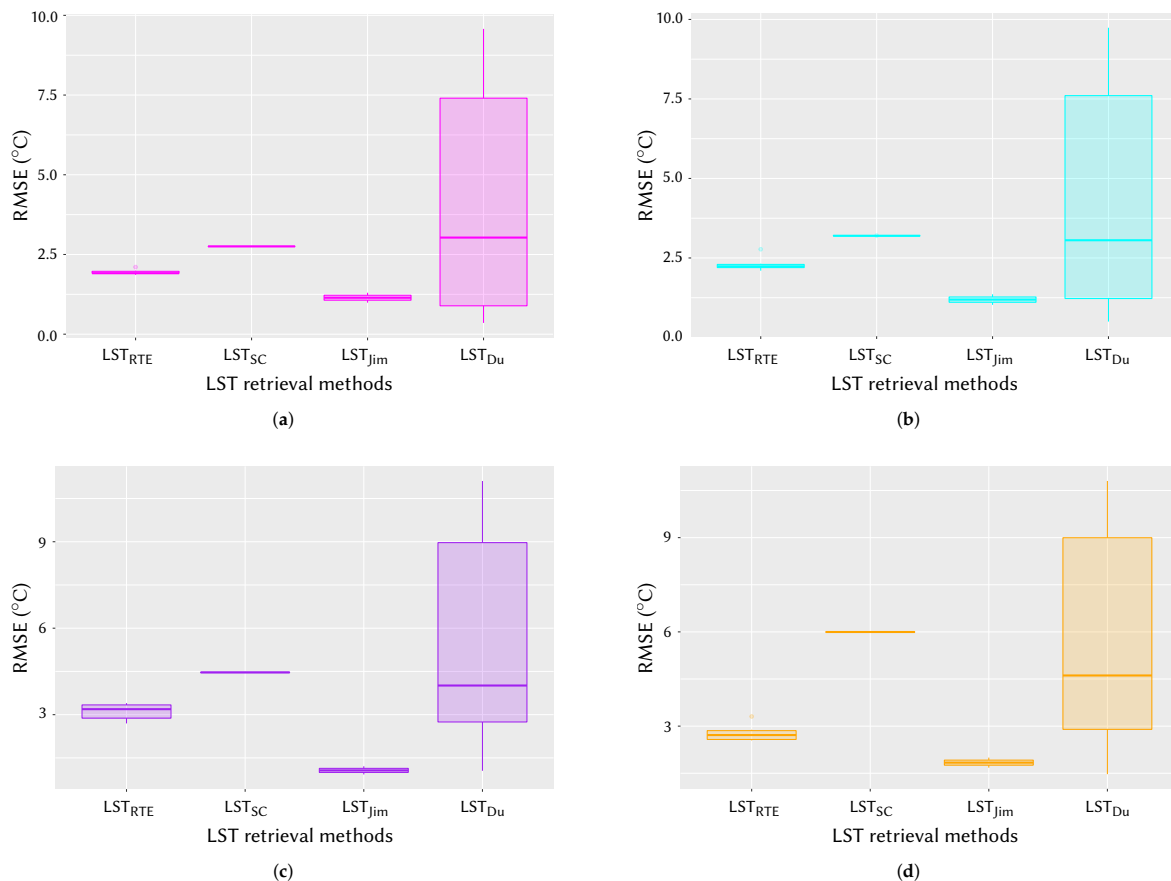
Figure 8. Box plots showing RMSEs of four LST retrieval algorithms as estimated on the Landsat 8 image of 21 February 2018.

(**a**)

(**b**)

(**c**)

(**d**)

(**e**)
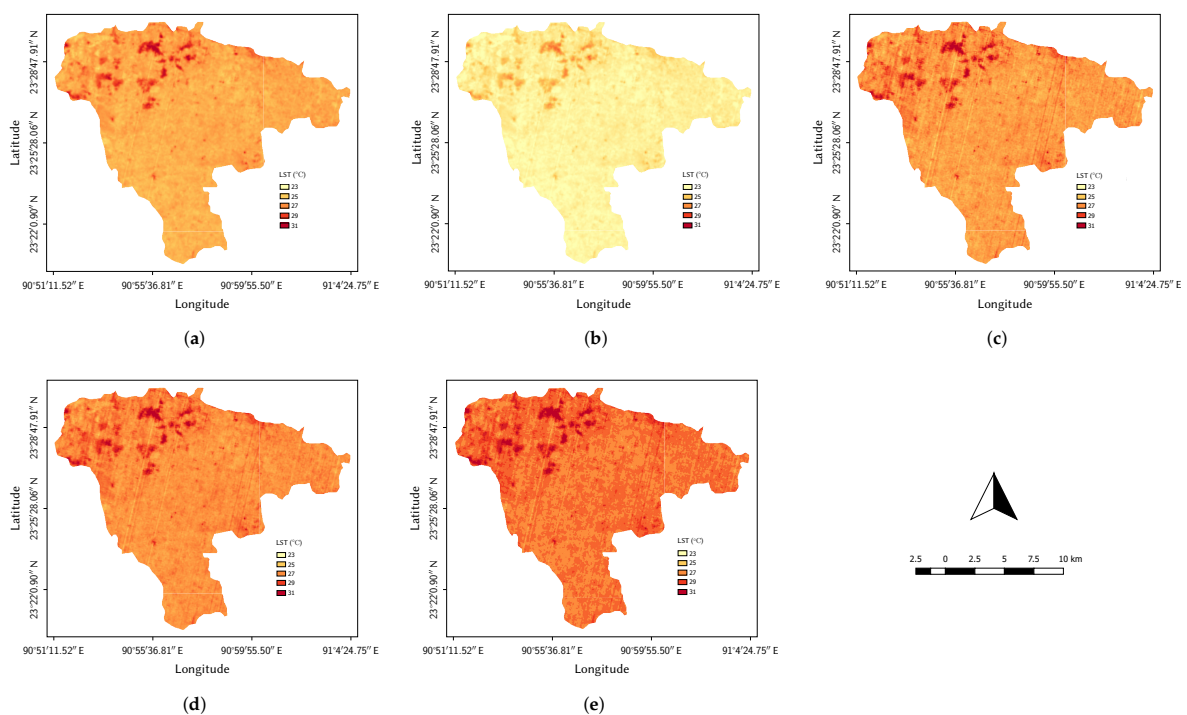
Figure 9. LST maps of the agricultural study area (Landsat 8 image of 21 February 2018): (**a**) RTE-based method using TIR band 10 ($\tau = 0.76$, $L_{up} = 1.94\,\mathrm{W\,m^{-2}\,sr^{-1}\,\mu m^{-1}}$, $L_{down} = 3.19\,\mathrm{W\,m^{-2}\,sr^{-1}\,\mu m^{-1}}$), (**b**) Single-Channel algorithm using TIR band 10 ($w = 2.0\,\mathrm{g\,cm^{-2}}$), (**c**) Du et al.'s [40] Split-Window algorithm ($w = 0.0$ to $6.3\,\mathrm{g\,cm^{-2}}$), (**d**) Jiménez-Muñoz et al.'s [37] Split-Window algorithm ($w = 1.0\,\mathrm{g\,cm^{-2}}$), and (**e**) using the ATCOR module (the reference LST).

Similar intercomparison study was performed on four additional Landsat 8 images. The box plots representing the intercomparison results of four LST algorithms on Landsat 8 images of different dates are shown in Figure 10. As seen in this figure, the LST results of different algorithms obtained for several Landsat 8 images agree with the results obtained for Landsat 8 image of 21 February 2018 (see Figure 8).

Figure 10. Box plots showing RMSEs of four LST retrieval algorithms as obtained from four Landsat 8 images: (**a**) 4 January 2018 image, (**b**) 20 January 2018 image, (**c**) 9 March 2018 image, and (**d**) 25 March 2018 image.

Considering all five Landsat 8 images used in this intercomparison study, the average RMSE is found to be $2.47\,^\circ$C for the LST_{RTE} method; $4.11\,^\circ$C for LST_{SC}; $1.19\,^\circ$C for LST_{Jim}; and $1.50\,^\circ$C for the LST_{Du} algorithm (not shown in Table). It can be mentioned here that the w values retrieved from the NCEP database were different for Landsat 8 images of different dates (see Table 8). The corresponding w ranges were taken into consideration for the calculation of LSTs with different methods.

4.6. Variation in LST Results due to Wrong Amount of Water Vapor Contents

The Single-Channel algorithm and the two Split-Window algorithms used to retrieve LST from Landsat 8 are dependent on atmospheric water vapor content (w). Therefore, it is necessary to study their performance in different amounts of w. To perform this study, we retrieved LSTs for the Single-Channel algorithm and Jiménez-Muñoz et al.'s Split-Window algorithm for w amount up to $4.5\,\mathrm{g\,cm}^{-2}$, that is, three more observations than it is seen in Table 7. For Du et al.'s Split-Window algorithm, we used the LSTs retrieved for all w sub-ranges.

The variation in RMSEs of LST results for three algorithms was plotted against varied amount of w as shown in Figure 11. Since the algorithms for LST_{SC} and LST_{Jim} require direct input of w, the two plots (Figure 11a,b) share w values in same intervals. On the other hand, RMSE variation for the LST_{Du} algorithm is shown with several sub-ranges of w (Figure 11c).
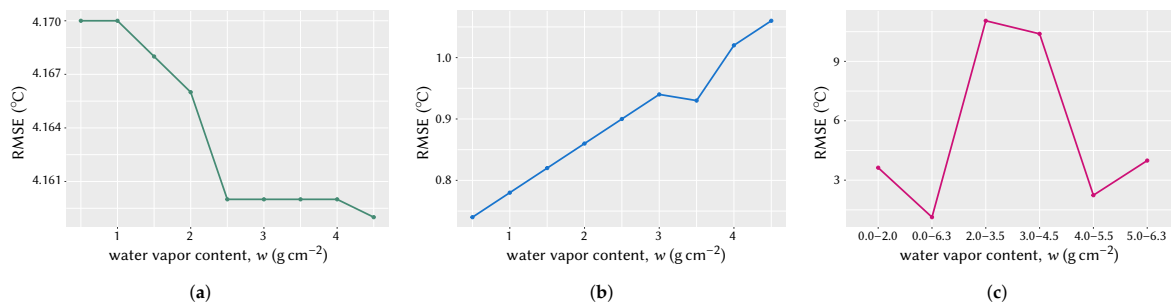
Figure 11. Variation of RMSEs with water vapor content: (**a**) using Single-Channel algorithm for Landsat 8 TIR band 10, (**b**) Split-Window algorithm and coefficients according to Jiménez-Muñoz et al., and (**c**) Split-Window algorithm and coefficients according to Du et al.

As seen in Figure 11a, for LST_{SC} the RMSE decreases with increasing w, whereas in Figure 11b, RMSE for LST_{Jim} increases with increasing w. The decrease of RMSE for LST_{SC} in lower w is quite abrupt compared to its change in higher w (Figure 11a). For the LST_{Jim}, the increase in RMSE with increasing w is almost constant (Figure 11b). On the other hand, for LST_{Du} (Figure 11c), LST error is very high when $w = 0.0$ to $4.5\,\mathrm{g\,cm^{-2}}$; it is lowest when w lies in 4.0 to $6.3\,\mathrm{g\,cm^{-2}}$; it is considerably better when $w = 0.0$ to $6.3\,\mathrm{g\,cm^{-2}}$, that is, algorithm coefficients for the entire w range. It is understandable from these plots that the use of wrong w value may result in unacceptable LST estimation, especially for the LST_{Du} algorithm. Therefore, it is very important to estimate the w of the study area with great precision.

4.7. Cross-Validation and Intercomparison of Landsat 8 LSTs Against MODIS Daily LSTs

As mentioned previously, MODIS daily LSTs for the study area were extracted using the A$\rho\rho$EEARS online tool. We considered the nearest available LSTs compared with Landsat 8 images of different dates used in this study. Since there are missing values for daily LSTs due to the effects of clouds and other atmospheric conditions, we retrieved MODIS LSTs for the dates of: (a) 5 January 2018, (b) 21 January 2018, (c) 22 February 2018, (d) 10 March 2018, and (e) 26 March 2018. The statistical values including the median and mean MODIS LSTs retrieved for these dates are presented in Figure 12 using box plots.

For cross-validation of Landsat 8 LSTs that were retrieved with four algorithms, as well as with the ATCOR module, the MODIS daily LSTs were converted into °C unit from K unit. Then, LST mean bias was computed for each Landsat 8 LST retrieval method against MODIS mean LST. The cross-validation and intercomparison results between Landsat 8 and MODIS daily LSTs are presented in Table 8. The Landsat 8 mean LST is denoted with LST_{L8}, MODIS mean LST with LST_{MOD}, and the mean LST bias between them is denoted with $Bias_{MOD–L8}$.

As seen in Table 8, the mean bias ($Bias_{MOD–L8}$) between LST_{L8} and LST_{MOD} is always lower for the LST_{Jim} algorithm among four Landsat 8 LST algorithms. The LST_{Du} algorithm performs very close to the LST_{Jim} method. The LST_{RTE} shows higher LST bias while the LST_{SC} has the highest bias among these four methods. It suggests that the best performing LST retrieval method for Landsat 8 is the LST_{Jim} Split-Window algorithm, with LST_{Du} method being the next, and LST_{RTE} having better performance than the LST_{SC} method. These cross-validation and intercomparison results agree with the intercomparison results obtained for different Landsat 8 LST methods when validated against LST_{ref} (see Section 4.5). It also reveals that the reference LST estimated from ATCOR module (LST_{ref}) performs efficiently showing a very small mean bias (from -0.58 to $-0.29\,°C$) for most images and the lowest mean bias for the first three Landsat 8 images (Table 8) used in this study (the only exception is the Landsat 8 image of 25 March 2018 with its corresponding MODIS daily LST where the mean bias is considerably higher).
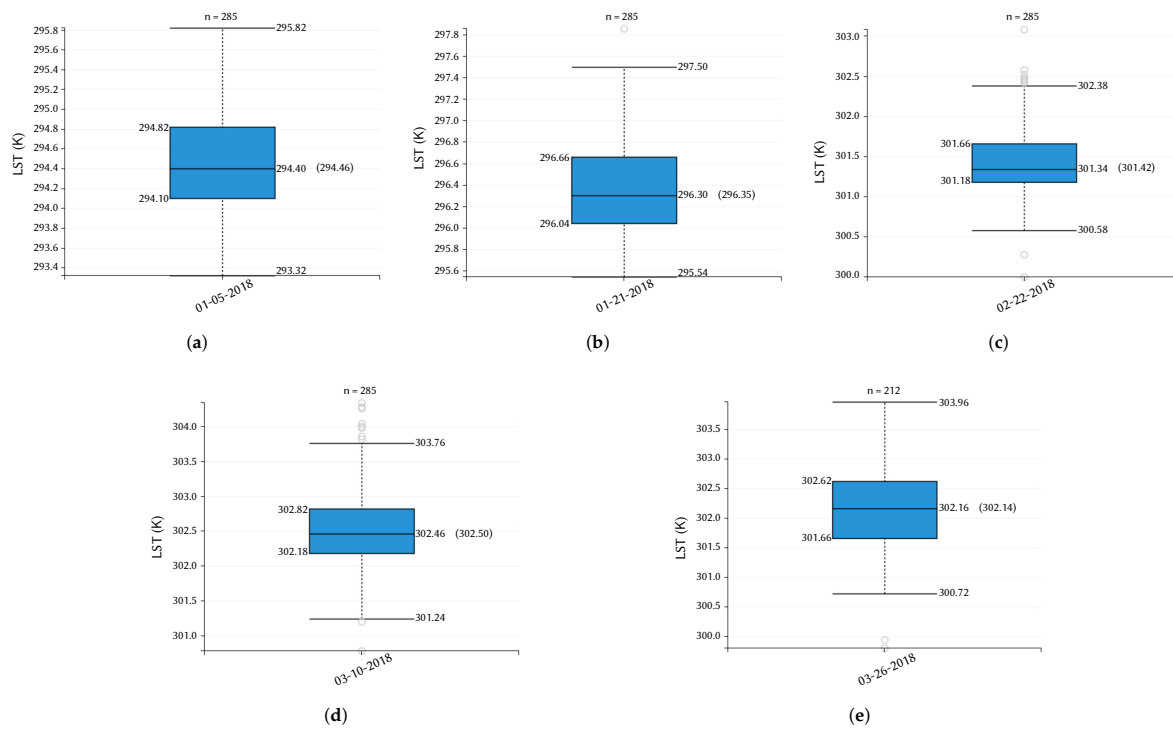
Figure 12. Box plots representing daily LSTs retrieved from the Terra MODIS images of different dates: (**a**) 5 January 2018 image, (**b**) 21 January 2018 image, (**c**) 22 February 2018 image, (**d**) 10 March 2018 image, and (**e**) 26 March 2018 image. The parameter *n* indicates the total number of values/pixels; the boxes show the interquartile range (IQR) along with median, mean (in parentheses) values; the whiskers represent the lowest and highest datum within 1.5 IQR of the lower- and upper-quartile, respectively (all LST values are in K unit).

Table 8. Cross-validation and intercomparison results of Landsat 8 LSTs retrieved with four algorithms and with the Atmospheric and Topographic CORection (ATCOR) module against Terra MODIS LSTs. All LST values are in °C; image acquisition dates are in yy-mm-dd format. Notations for different LST retrieval methods from Landsat 8 data are the same as in previous sections.

	Landsat 8 LSTs			Terra MODIS LSTs		
Image Date	**LST Methods**	**MEAN LST$_{L8}$**	**w (g cm^{-2})**	**Image Date**	**MEAN LST$_{MOD}$**	**Bias$_{MOD-L8}$**
2018-01-04	LST$_{RTE}$	19.65	0.5–2.0	2018-01-05	21.31	1.66
	LST$_{SC}$	18.84				2.47
	LST$_{Jim}$	20.56				0.75
	LST$_{Du}$	19.67				1.64
	LST$_{ref}$	21.60				−0.29
2018-01-20	LST$_{RTE}$	21.31	0.5–2.0	2018-01-21	23.20	1.89
	LST$_{SC}$	20.41				2.79
	LST$_{Jim}$	22.54				0.66
	LST$_{Du}$	21.67				1.53
	LST$_{ref}$	23.58				−0.38
2018-02-21	LST$_{RTE}$	25.64	1.5–3.0	2018-02-22	28.27	2.63
	LST$_{SC}$	23.66				4.61
	LST$_{Jim}$	26.98				1.29
	LST$_{Du}$	26.72				1.55
	LST$_{ref}$	27.80				0.47
2018-03-09	LST$_{RTE}$	26.89	1.0–2.5	2018-03-10	29.35	2.46
	LST$_{SC}$	25.51				3.84
	LST$_{Jim}$	28.97				0.38
	LST$_{Du}$	28.94				0.41
	LST$_{ref}$	29.93				−0.58

Table 8. *Cont.*

	Landsat 8 LSTs			Terra MODIS LSTs		
Image Date	LST Methods	MEAN LST$_{L8}$	w (g cm^{-2})	Image Date	MEAN LST$_{MOD}$	Bias$_{MOD-L8}$
2018-03-25	LST$_{RTE}$	28.93	3.0–4.5	2018-03-26	28.99	0.06
	LST$_{SC}$	25.70				3.29
	LST$_{Jim}$	29.74				−0.75
	LST$_{Du}$	30.23				−1.24
	LST$_{ref}$	31.66				−2.67

5. Conclusions

Landsat 8 data are great sources of high resolution remote sensing images with two thermal bands that can be efficiently used to retrieve LST. An intercomparison study among the existing LST algorithms for Landsat 8 was performed against ATCOR-derived reference LSTs and A$\rho\rho$EEARS-derived Terra MODIS daily LSTs. According to the observation of this study, the Single-Channel algorithm can be used in LST retrieval for Landsat 8 images, but use of a good Split-Window algorithm has the potential of ensuring greater accuracy. The challenges with a good, practical, and feasible Split-Window algorithm development can be the precise estimation of coefficient values and determination of atmospheric water vapor content of the study area.

Taking all Landsat 8 images used in this study under consideration against reference LST, the RTE-based method (LST$_{RTE}$) gives LST results better than the Single-Channel method (LST$_{SC}$) with an average RMSE = 2.47 °C; but it (LST$_{RTE}$) performs worse compared to the Split-Window algorithms. Since the RTE-based direct algorithm depends heavily on various atmospheric parameters, precision calculation of those parameters can be the determinant of LST accuracy. The use of NCEP database and MODTRAN codes through the online atmospheric correction calculator seems promising for this method.

The LST results with Single-Channel algorithm provide larger RMSE (average RMSE = 4.11 °C) than the RTE-based method. In contrast, Jiménez-Muñoz et al.'s Split-Window Algorithm (LST$_{Jim}$) shows the best performance (average RMSE = 1.19 °C) among other methods. These two LST algorithms (LST$_{SC}$ and LST$_{Jim}$) can be chosen when: (a) actual water vapor content is precisely measured, and (b) other atmospheric parameters are not available as they are not necessary in these two methods. Especially for the Single-Channel algorithm, it is not advisable to use this method for images that have more than one thermal band.

The Du et al.'s Split-Window Algorithm (LST$_{Du}$) with its coefficients available for w range 0.0 to 6.3 g cm^{-2} can be applied for an area where the actual amount of water vapor content cannot be determined or very uncertain for precision determination. The reasons behind this recommendation are: (a) this algorithm gives good LST results compared to other methods with RMSE = 1.50 °C as found in this study, and (b) other three LST algorithms require either the direct input of water vapor content (LST$_{SC}$ and LST$_{Jim}$ methods) or several atmospheric parameters (LST$_{RTE}$ method). On the other hand, the potential problem with this method is that the w range of 0.0 to 6.3 g cm^{-2} is too much of generalization and could give unsatisfactory results in areas with different atmospheric conditions than observed in this study.

The cross-validation and intercomparison results of Landsat 8 LSTs with different algorithms against MODIS daily LSTs were found to agree with the intercomparison results against reference LSTs. The mean bias (Bias$_{MOD-L8}$) here for the LST$_{Jim}$ algorithm was found always lower compared to other Landsat 8 LST algorithms. The ATCOR-derived Landsat 8 LST was found with even lower Bias$_{MOD-L8}$ for the first three images used in this study revealing that the ATCOR-derived LSTs can be used as references for the indirect verification of Landsat 8 LST algorithms.

The in situ LSTs were not available in this study; therefore, ground validation of Landsat 8 LST algorithms was not performed. Monitoring of in situ LST data with precision radiosounding instruments or radiometers correcting for the effects of emissivity and synchronizing with the actual

time of satellite overpass could be taken into consideration to perform the ground validation of LST algorithms.

Although the NCEP atmospheric profile database was found providing with good estimation of atmospheric parameters, other databases (e.g., TIGR, GAPRI, CLAR, etc.) can be used to study their relative performances. Land surface emissivity from MODIS or ASTER remote sensing images can be compared against NDVI-based emissivity in the retrieval of precision LST. Cross-validation of LST from Landsat 8 with MODIS daily LST retrieved using the AρρEEARS online tool was found promising in the intercomparison study of different Landsat 8 LST algorithms. Other sources of remote sensing data can be used in the cross-validation study to further enhance the verification of Landsat 8 LST products.

Author Contributions: Conceptualization, M.Q.U.S.; Data curation, M.Q.U.S. and T.W.; Formal analysis, T.W.; Methodology, M.Q.U.S.; Supervision, T.W.; Validation, T.W.; Visualization, M.Q.U.S.; Writing—original draft, M.Q.U.S.; Writing—review & editing, M.Q.U.S. and T.W. All authors have read and agreed to the published version of the manuscript.

References

1. Wan, Z.; Dozier, J. Land-surface temperature measurement from space: Physical principles and inverse modeling. *IEEE Trans. Geosci. Remote. Sens.* **1989**, *27*, 268–278.

2. Voogt, J.A.; Oke, T. Thermal remote sensing of urban climates. *Remote. Sens. Environ.* **2003**, *86*, 370–384. [CrossRef]

3. Zhou, J.; Chen, Y.; Wang, J.; Zhan, W. Maximum Nighttime Urban Heat Island (UHI) Intensity Simulation by Integrating Remotely Sensed Data and Meteorological Observations. *IEEE J. Sel. Top. Appl. Earth Obs. Remote. Sens.* **2011**, *4*, 138–146. [CrossRef]

4. Eckmann, T.; Roberts, D.; Still, C. Using multiple endmember spectral mixture analysis to retrieve subpixel fire properties from MODIS. *Remote. Sens. Environ.* **2008**, *112*, 3773–3783. [CrossRef]

5. Merlin, O.; Duchemin, B.; Hagolle, O.; Jacob, F.; Coudert, B.; Chehbouni, G.; Dedieu, G.; Garatuza, J.; Kerr, Y. Disaggregation of MODIS surface temperature over an agricultural area using a time series of Formosat-2 images. *Remote. Sens. Environ.* **2010**, *114*, 2500–2512. [CrossRef]

6. Sandholt, I.; Rasmussen, K.; Andersen, J. A simple interpretation of the surface temperature/vegetation index space for assessment of surface moisture status. *Remote. Sens. Environ.* **2002**, *79*, 213–224. [CrossRef]

7. Zhan, W.; Chen, Y.; Zhou, J.; Wang, J.; Liu, W.; Voogt, J.A.; Zhu, X.; Quan, J.; Li, J. Disaggregation of remotely sensed land surface temperature: Literature survey, taxonomy, issues, and caveats. *Remote. Sens. Environ.* **2013**, *131*, 119–139. [CrossRef]

8. Crow, W.T.; Wood, E. The assimilation of remotely sensed soil brightness temperature imagery into a land surface model using Ensemble Kalman filtering: a case study based on ESTAR measurements during SGP97. *Adv. Water Resour.* **2003**, *26*, 137–149. [CrossRef]

9. Kustas, W.; Anderson, M.C. Advances in thermal infrared remote sensing for land surface modeling. *Agric. For. Meteorol.* **2009**, *149*, 2071–2081. [CrossRef]

10. Shwetha, H.; Kumar, D.N. Prediction of Land Surface Temperature Under Cloudy Conditions Using Microwave Remote Sensing and ANN. *Aquat. Procedia* **2015**, *4*, 1381–1388. [CrossRef]

11. Aslan, N.; Koc-San, D. Analysis of relationship between urban heat island effect and land use/cover type using landsat 7 ETM+ and landsat 8 oli images. *Int. Arch. Photogramm. Remote. Sens. Spat. Inf. Sci.* **2016**, *41*, 821–828. [CrossRef]

12. Holmes, T.R.; De Jeu, R.A.M.; Owe, M.; Dolman, H. Land surface temperature from Ka band (37 GHz) passive microwave observations. *J. Geophys. Res. Space Phys.* **2009**, *114*. [CrossRef]

13. Meier, F.; Scherer, D.; Richters, J.; Christen, A. Atmospheric correction of thermal-infrared imagery of the 3-D urban environment acquired in oblique viewing geometry. *Atmos. Meas. Tech.* **2011**, *4*, 909–922. [CrossRef]

14. Li, Z.-L.; Tang, B.-H.; Wu, H.; Ren, H.; Yan, G.; Wan, Z.; Trigo, I.F.; Sobrino, J.A. Satellite-derived land surface temperature: Current status and perspectives. *Remote. Sens. Environ.* **2013**, *131*, 14–37. [CrossRef]

15. Lakshmi, V.; Czajkowski, K.; Dubayah, R.; Susskind, J. Land surface air temperature mapping using TOVS and AVHRR. *Int. J. Remote. Sens.* **2001**, *22*, 643–662. [CrossRef]

16. Zhou, J.; Li, J.; Zhang, L.; Hu, D.; Zhan, W. Intercomparison of methods for estimating land surface temperature from a Landsat-5 TM image in an arid region with low water vapour in the atmosphere. *Int. J. Remote. Sens.* **2012**, *33*, 2582–2602. [CrossRef]

17. Stisen, S.; Sandholt, I.; Nørgaard, A.; Fensholt, R.; Eklundh, L. Estimation of diurnal air temperature using MSG SEVIRI data in West Africa. *Remote. Sens. Environ.* **2007**, *110*, 262–274. [CrossRef]

18. Vancutsem, C.; Ceccato, P.; Dinku, T.; Connor, S.J. Evaluation of MODIS land surface temperature data to estimate air temperature in different ecosystems over Africa. *Remote. Sens. Environ.* **2010**, *114*, 449–465. [CrossRef]

19. Jang, J.-D.; Viau, A.A.; Anctil, F. Neural network estimation of air temperatures from AVHRR data. *Int. J. Remote. Sens.* **2004**, *25*, 4541–4554. [CrossRef]

20. Dash, P.; Göttsche, F.-M.; Olesen, F.-S.; Fischer, H. Land surface temperature and emissivity estimation from passive sensor data: Theory and practice-current trends. *Int. J. Remote. Sens.* **2002**, *23*, 2563–2594. [CrossRef]

21. Sobrino, J.A.; Jiménez-Muñoz, J.C.; Paolini, L. Land surface temperature retrieval from LANDSAT TM 5. *Remote Sens. Environ.* **2004**, *90*, 434–440. [CrossRef]

22. Feizizadeh, B.; Blaschke, T. Thermal remote sensing for land surface temperature monitoring: Maraqeh County, Iran. In Proceedings of the 2012 IEEE International Geoscience and Remote Sensing Symposium, Munich, Germany, 22–27 July 2012; pp. 2217–2220.

23. Fu, P.; Weng, Q. Consistent land surface temperature data generation from irregularly spaced Landsat imagery. *Remote. Sens. Environ.* **2016**, *184*, 175–187. [CrossRef]

24. Mallick, J.; Kant, Y.; Bharath, B.D. Estimation of land surface temperature over Delhi using Landsat-7 ETM+. *J. Indian Geophys. Union* **2008**, *12*, 131–140.

25. Sahana, M.; Ahmed, R.; Sajjad, H. Analyzing land surface temperature distribution in response to land use/land cover change using split window algorithm and spectral radiance model in Sundarban Biosphere Reserve, India. *Model. Earth Syst. Environ.* **2016**, *2*, 81. [CrossRef]

26. Banglapedia. Bangladesh Geography. Available online: http://en.banglapedia.org/index.php?title=Bangladesh_Geography (accessed on 19 March 2020).

27. BBC. Bangladesh Country Profile. Available online: https://www.bbc.com/news/world-south-asia-12650940 (accessed on 4 January 2018).

28. Ahmed, B.; Kamruzzaman; Zhu, X.; Rahman, S.; Choi, K. Simulating Land Cover Changes and Their Impacts on Land Surface Temperature in Dhaka, Bangladesh. *Remote Sens.* **2013**, *5*, 5969–5998. [CrossRef]

29. Raja, D.R. Spatial Analysis of Land Surface Temperature in Dhaka Metropolitan Area. *J. Bangladesh Instit. Plan.* **2012**, *5*, 151–167.

30. Roni, R. Surface Temperature and NDVI Generation and Relation between Them: Application of Remote Sensing. *Asian J. Eng. Technol. Innov.* **2013**, *1*, 8–13.

31. Sultana, S.H.; Ali, M.S.; Hena, M.A.; Rahman, M.M. A Simple Model of Mapping of Land Surface Temperature from Satellite Digital Images in Bangladesh. *Int. J. Inf. Technol. Comput. Sci.* **2013**, *1*, 51–57. [CrossRef]

32. Ara, S.; Islam, A.; Showkat, S. Effect of land-use intensity on surface temperature: A study on Chittagong city corporation area. In Proceedings of the 2016 5th International Conference on Informatics, Electronics and Vision (ICIEV), Dhaka, Bangladesh, 13–14 May 2016.

33. Masiello, G.; Serio, C.; De Feis, I.; Amoroso, M.; Venafra, S.; Trigo, I.F.; Watts, P. Kalman filter physical retrieval of surface emissivity and temperature from geostationary infrared radiances. *Atmos. Meas. Tech.* **2013**, *6*, 3613–3634. [CrossRef]

34. Masiello, G.; Serio, C.; Venafra, S.; Liuzzi, G.; Göttsche, F.; Trigo, I.F.; Watts, P. Kalman filter physical retrieval of surface emissivity and temperature from SEVIRI infrared channels: A validation and intercomparison study. *Atmos. Meas. Tech.* **2015**, *8*, 2981–2997. [CrossRef]

35. Grazia, M.; Liuzzi, G.; Masiello, G.; Serio, C.; Telesca, V.; Venafra, S. Surface parameters from SEVIRI observations through a Kalman filter approach: Application and evaluation of the scheme in Southern Italy. *Tethys: J. Weather. Clim. West. Mediterrania* **2016**, *13*, 3–10. [CrossRef]

36. Jiménez-Muñoz, J.C.; Sobrino, J.A. A generalized single-channel method for retrieving land surface temperature from remote sensing data. *J. Geophys. Res. Space Phys.* **2003**, *108*, D22. [CrossRef]

37. Jiménez-Muñoz, J.C.; Sobrino, J.A.; zen Skoković, D.; Mattar, C.; Cristóbal, J. Land Surface Temperature Retrieval Methods From Landsat-8 Thermal Infrared Sensor Data. *IEEE Geosci. Remote Sens. Lett.* **2014**, *11*, 1840–1843. [CrossRef]

38. Sobrino, J.A.; Li, Z.-L.; Stoll, M.P.; Becker, F. Multi-channel and multi-angle algorithms for estimating sea and land surface temperature with ATSR data. *Int. J. Remote Sens.* **1996**, *17*, 2089–2114. [CrossRef]

39. Wan, Z. New refinements and validation of the collection-6 MODIS land-surface temperature/emissivity product. *Remote. Sens. Environ.* **2014**, *140*, 36–45. [CrossRef]

40. Du, C.; Ren, H.; Qin, Q.; Meng, J.; Zhao, S. A Practical Split-Window Algorithm for Estimating Land Surface Temperature from Landsat 8 Data. *Remote Sens.* **2015**, *7*, 647–665. [CrossRef]

41. Yu, X.; Guo, X.; Wu, Z. Land Surface Temperature Retrieval from Landsat 8 TIRS—Comparison between Radiative Transfer Equation-Based Method, Split Window Algorithm and Single Channel Method. *Remote Sens.* **2014**, *6*, 9829–9852. [CrossRef]

42. Jiménez-Muñoz, J.C.; Cristobal, J.; Sobrino, J.A.; Soria, G.; Ninyerola, M.; Pons, X. Revision of the Single-Channel Algorithm for Land Surface Temperature Retrieval From Landsat Thermal-Infrared Data. *IEEE Trans. Geosci. Remote Sens.* **2009**, *47*, 339–349. [CrossRef]

43. Neteler, M. Estimating Daily Land Surface Temperatures in Mountainous Environments by Reconstructed MODIS LST Data. *Remote Sens.* **2010**, *2*, 333–351. [CrossRef]

44. AppEEARS Team. Application for Extracting and Exploring Analysis Ready Samples (AppEEARS) Ver. 2.22. Available online: https://lpdaacsvc.cr.usgs.gov/appeears/ (accessed on 25 May 2019).

45. Wan, Z.; Hook, S.; Hulley, G. MOD11A1 MODIS/Terra Land Surface Temperature/Emissivity Daily L3 Global 1km SIN Grid V006. Available online: https://lpdaac.usgs.gov/products/mod11a1v006/ (accessed on 19 March 2020).

46. Montanaro, M.; Gerace, A.; Lunsford, A.; Reuter, D. Stray Light Artifacts in Imagery from the Landsat 8 Thermal Infrared Sensor. *Remote Sens.* **2014**, *6*, 10435–10456. [CrossRef]

47. Malakar, N.K.; Hulley, G.C.; Hook, S.J.; Laraby, K.; Cook, M.; Schott, J.R. An Operational Land Surface Temperature Product for Landsat Thermal Data: Methodology and Validation. *IEEE Trans. Geosci. Remote Sens.* **2018**, *56*, 5717–5735. [CrossRef]

48. U.S. Geological Survey. Landsat 8 (L8) Data Users Handbook, Version 2.0. Available online: https://www.usgs.gov/land-resources/nli/landsat/landsat-8-data-users-handbook (accessed on 19 March 2020).

49. Wikipedia. Geography of Bangladesh. Available online: https://en.wikipedia.org/wiki/Geography_of_Bangladesh (accessed on 1 February 2019).

50. Wikipedia. Comilla District. Available online: https://en.wikipedia.org/wiki/Comilla_District (accessed on 1 February 2019).

51. Banglapedia. Comilla District. Available online: http://en.banglapedia.org/index.php?title=Comilla_District (accessed on 1 February 2019).

52. Banglapedia. Chandina Upazila. Available online: http://en.banglapedia.org/index.php?title=Chandina_Upazila (accessed on 1 February 2019).

53. Parastatidis, D.; Mitraka, Z.; Chrysoulakis, N.; Abrams, M. Online Global Land Surface Temperature Estimation from Landsat. *Remote Sens.* **2017**, *9*, 1208. [CrossRef]

54. Wan, Z.M.; Dozier, J. A generalized split-window algorithm for retrieving land-surface temperature from space. *IEEE Trans. Geosci. Remote Sens.* **1996**, *34*, 892–905.

55. Rozenstein, O.; Qin, Z.; Derimian, Y.; Karnieli, A. Derivation of Land Surface Temperature for Landsat-8 TIRS Using a Split Window Algorithm. *Sensors* **2014**, *14*, 5768–5780. [CrossRef] [PubMed]

56. Mattar, C.; Durán-Alarcón, C.; Jiménez-Muñoz, J.C.; Santamaría-Artigas, A.; Olivera-Guerra, L.; Sobrino, J.A. Global Atmospheric Profiles from Reanalysis Information (GAPRI): A new database for earth surface temperature retrieval. *Int. J. Remote Sens.* **2015**, *36*, 5045–5060. [CrossRef]

57. Barsi, J.A.; Schott, J.R.; Palluconi, F.D.; Hook, S.J. Validation of a web-based atmospheric correction tool for single thermal band instruments. In Proceedings of the Optics and Photonics, San Diego, CA, USA, 31 July–4 August 2005.

58. Jiménez-Muñoz, J.C.; Sobrino, J.A. Split-Window Coefficients for Land Surface Temperature Retrieval From Low-Resolution Thermal Infrared Sensors. *IEEE Geosci. Remote Sens. Lett.* **2008**, *5*, 806–809. [CrossRef]

59. NASA Landsat Science. Spectral Response of the Thermal Infrared Sensor. Available online: https://landsat.gsfc.nasa.gov/preliminary-spectral-response-of-the-thermal-infrared-sensor/ (accessed on 19 March 2020).

60. Barsi, J.A.; Barker, J.L.; Schott, J.R. An Atmospheric Correction Parameter Calculator for a Single Thermal Band Earth-Sensing Instrument. In Proceedings of the 2003 IEEE International Geoscience and Remote Sensing Symposium, Toulouse, France, 21–25 July 2003.

61. Coll, C.; Galve, J.M.; Sánchez, J.M.; Caselles, V. Validation of Landsat-7/ETM+ Thermal-Band Calibration and Atmospheric Correction With Ground-Based Measurements. *IEEE Trans. Geosci. Remote Sens.* **2010**, *48*, 547–555. [CrossRef]

62. Galve, J.M.; Sánchez, J.M.; Coll, C.; Villodre, J. A New Single-Band Pixel-by-Pixel Atmospheric Correction Method to Improve the Accuracy in Remote Sensing Estimates of LST. Application to Landsat 7-ETM+. *Remote Sens.* **2018**, *10*, 826. [CrossRef]

63. Sobrino, J.A.; Raissouni, N. Toward remote sensing methods for land cover dynamic monitoring: Application to Morocco. *Int. J. Remote Sens.* **2000**, *21*, 353–366. [CrossRef]

64. Carlson, T.N.; Ripley, D.A. On the Relation between NDVI, Fractional Vegetation Cover, and Leaf Area Index. *Remote Sens. Environ.* **1997**, *62*, 241–252. [CrossRef]

65. Avdan, U.; Jovanovska, G. Algorithm for Automated Mapping of Land Surface Temperature Using LANDSAT 8 Satellite Data. *J. Sens.* **2016**, *2016*. [CrossRef]

66. Sobrino, J.A.; Jiménez-Muñoz, J.C.; Sòria, G.; Romaguera, M.; Guanter, L.; Moreno, J.; Plaza, A.; Martinez, P. Land Surface Emissivity Retrieval From Different VNIR and TIR Sensors. *IEEE Trans. Geosci. Remote Sens.* **2008**, *46*, 316–327. [CrossRef]

67. Ren, H.; Liu, R.; Yan, G.; Li, Z.L.; Qin, Q.; Liu, Q.; Nerry, F. Performance evaluation of four directional emissivity analytical models with thermal SAIL model and airborne images. *Opt. Express* **2015**, *23*, A346–A360. [CrossRef]

68. Ye, X.; Ren, H.; Liu, R.; Qin, Q.; Liu, Y.; Dong, J. Land Surface Temperature Estimate From Chinese Gaofen-5 Satellite Data Using Split-Window Algorithm. *IEEE Trans. Geosci. Remote Sens.* **2017**, *55*, 5877–5888. [CrossRef]

69. Sobrino, J.A.; Caselles, V.; Becker, F. Significance of the remotely sensed thermal infrared measurements obtained over a citrus orchard. *ISPRS J. Photogramm. Remote Sens.* **1990**, *44*, 343–354. [CrossRef]

70. QGIS Development Team. QGIS. Available online: https://qgis.org/en/site/ (accessed on 19 March 2020).

71. R Core Team. R: A Language and Environment for Statistical Computing. Available online: https://www.gbif.org/zh/tool/81287/r-a-language-and-environment-for-statistical-computing (accessed on 19 March 2020).

72. Hijmans, R.J.; van Etten, J. Raster: Geographic Data Analysis and Modeling. Version 2.6-7. Available online: https://rdrr.io/cran/raster/ (accessed on 19 March 2020).

73. Bivand, R.; Keitt, T.; Rowlingson, B.; Pebesma, E.; Sumner, M.; Hijmans, R.; Rouaul, E.; Warmerdam, F.; Ooms, J.; Rundel, C. rgdal: Bindings for the Geospatial Data Abstraction Library. Version 1.3-4. Available online: https://mran.microsoft.com/snapshot/2018-08-31/web/packages/rgdal/index.html (accessed on 19 March 2020).

74. Wickham, H. *ggplot2: Elegant Graphics for Data Analysis*, 2nd ed.; Springer: New York, NY, USA, 2016.

75. Kuhn, M. caret: Classification and Regression Training. Version 6.0-81. Available online: https://rdrr.io/cran/caret/ (accessed on 19 March 2020).